

1 abstract

The impact of structure on water is an important and practical issue in ocean engineering. For some cases, the influence of air on the impact characteristics is non-negligible. In particular, when the flat-bottomed structure impacts on water such as the emergency landing on the water of an aircraft and helicopter, the air cushion will be formed which buffers the impact of the structure, thereby reducing its slamming load. In this paper, considering the advantages of the Riemann solver in dealing with discontinuities, a multiphase Riemann-SPH method using the PVRS Riemann solver is applied to analyze the air-cushion effect and slamming load in water entry problems. To reduce the numerical dissipation led by the Riemann solver, a dissipation limiter for the PVRS Riemann solver is given. Through the test of the water slamming of the plate, the accuracy and convergence of the adopted method are firstly validated. Then, the influences of the air cushion and the plate length on the slamming load are discussed. Finally, a complex engineering problem, i.e., the slamming of the LNG tank insulation panel is simulated, and the influences of the impact velocity and deadrise angle on slamming load characteristics are analyzed.

在海洋工程中，结构物对水的冲击是重要且实际的问题。在某些情况下，空气流动对碎击特性的影响是不可忽略的。特别是平底结构物对水的碎击，例如飞机和直升机的水面迫降时，会形成缓解结构物冲击的气垫，从而减小碎击载荷。本文基于黎曼求解器善于处理非连续性问题的优势，应用一种使用PVRS 黎曼求解器的多相黎曼-SPH 方法分析研究了入水问题中的气垫效应和碎击载荷。为了减少由黎曼求解器引起的数值耗散，给出了 PVRS 黎曼求解器的耗散限制器。通过板的水击试验，首次验证了所采用方法的准确性和收敛性。随后讨论了气垫和板长对碎击载荷的影响。最后模拟了一个复杂的工程问题，即 LNG 船绝缘板的碎击模拟，并研究了碎击速度和静升角对碎击载荷特性的影响。

2 introduction

The study of slamming load between water and structures is of great significance in engineering for a long time, and the magnitude of slamming load is usually difficult to predict due to the complexity of the problem. For some cases, the influence of air is non-negligible for the impact characteristics since the existence of the air-cushion effect in water entry can buffer the impact of the structure, thereby reducing the slamming load. To investigate these slamming loads, many researchers have performed a lot of remarkable work. A pioneering experimental research carried out by Chuang (1966) focused on the impact of the wedges with different deadrise angles, which firstly demonstrated that compared with the classical Wagner theory (Über, 1932), the air cushion can considerably reduce the slamming loads in practice. Subsequently, Lewison (1968) pointed out that, the air would be forced into the water during the impact when the deadrise angle is small enough, implying the coalescence between the water and vapour. In addition, in the experiments on free-falling plates studied by Okada and Sumi (2000), it was found that the effects of impact would be classified according to the impact angle. For the cases with impact angles greater than 4° , the “Wagner-type” impact pressure was large and very sharp both in time and space. For the cases with impact angles smaller than 4° , the impact pressure

becomes much smaller and smoother owing to the cushioning effect of air.

长期以来，水和结构物间的砰击载荷的研究在工程中具有重要意义，并且由于问题的复杂性，砰击载荷的大小通常难以预测。在某些情况下，空气对与砰击特性的影响是不可忽略的，因为入水处气垫效应的存在能缓冲结构物的砰击，从而减小砰击载荷。为了研究这种砰击载荷，很多研究者做出了许多卓越的工作。由 Chuang(1996) 提出的一项开创性的实验研究，重点研究了不同静升角的楔形块的砰击，首次证明了与经典瓦格纳理论相比，在实践中气垫可以显著减小砰击载荷。随后，Lewison(1968) 指出，当静升角足够小时，空气可能会被迫进入水中，这意味着水和蒸汽的结合。此外，在 Okada 和 Sumi(2000) 研究的自由落体板实验中，发现砰击类型可根据砰击角度分类。在砰击角度大于四度时，在时间和空间上瓦格纳类型的砰击压力都非常大且尖锐。在砰击角度小于四度时，由于空气的缓冲作用，砰击压力会变得更小且更平滑。

With the rapid development of the computational fluid dynamics, many numerical research have been conducted to analyze the slamming loads. Ng and Kot (1992) used the volume-of-fluid (VOF) method to study the impact of the flat plate, but the incompressible air phase was set in their model. They found that before the impact, the air could make the water surface deformed. In the work of Yang and Qiu (2012), some problems of water slamming, including the impact of the plate on water, were studied by finite difference method (FDM). In their results, the slamming pressure was basically consistent with the experimental data, indicating the cushioning effect of air was captured. Moreover, Ma et al. (2014) established the compressible multiphase model of water slamming based on the Finite Volume Method (FVM) to solve the problems of strongly entrained wave impact.

随着 CFD 的快速发展，涌现出了大量对砰击载荷的数值研究。Ng 和 Kot(1992) 基于 VOF 方法研究了平板冲击问题，但是在他们的模型中空气被设置成不可压流体。他们发现在砰击前空气会使水面变形。在 Yang 和 Qiu(2012) 的工作中，他们使用了 FDM 方法研究了一些水击问题，包括板对水的砰击问题。研究发现砰击压力基本上和实验数据一致，这表明验证了空气的缓冲作用的存在。Moreover, Ma et al.(2014) 建立了基于 FVM 方法的水击可压缩多相求解器，用以求解强卷吸波问题。

In recent years, particle methods have shown great developments in both theories and applications. Thanks to its Lagrangian characteristics, the particle method is more flexible to deal with the interface compared to the above mesh methods and it is very suitable to solve the problems involving large deformations including the problem of free-surface flows (Antuono et al., 2010; Lind et al., 2012; Zhang and Liu, 2018; Kazemi et al., 2020), multiphase flows (Yang et al., 2020; Gong et al., 2016; Chen et al., 2015; Sun et al., 2021a, 2021b) and fluid-structure couplings (Khayyer et al., 2021; Zhang et al., 2019; Nasar et al., 2019; Liu and Zhang, 2019; Liu et al., 2014). Many studies on impact problems have been carried out by particle methods (see e.g. Gong et al., 2019; Wang et al., 2019a; Sun et al., 2018). However, there are few studies focusing on the cushioning effect of the trapped air for impact problems in particle methods. Lind et al. (2015) proposed an incompressible-compressible SPH model to predict the slamming pressure peak when the flat plate impacts on waves of different slopes. In their numerical model, the air is solved by weakly compressible SPH (WCSPH) method, and the

water is solved by incompressible SPH (ISPH) method. Khayyer and Gotoh (2016) proposed another compressible-incompressible multiphase model based on the projection-based particle method to predict the slamming load. This method can be considered as the extended version of Moving Particle Semi-implicit (MPS) method, and their numerical results show good agreement with experimental data. In addition, Marrone et al. (2018) studied the impact pressure of the flat panels with small deadrise angles, and the ditching problem including a large horizontal velocity component is discussed.

近年来，粒子方法在理论和应用方面均展现出巨大的发展。得益于其拉格朗日特性，粒子方法处理表面比上述网格方法更灵活，并且非常适合求解大变形问题，包括自由表面流问题 (Antuono et al.,2010;Lind et al.,2012;Zhang and Liu,2018;Kazemi et al.,2020)，多相流问题 (Yang et al.,2020;Gong et al.,2016;Chen et al.,2015;Sun et al.,2021a,2021b) 和流固耦合 (Khayyer et al.,2021;Zhang et al.,2019;Nasar et al.,2019;Liu and Zhang,2019;Liu et al.,2014)。许多关于冲击问题的研究都是通过粒子方法进行 (见 Gong et al.,2019;Wang et al.,2019a;Sun et al.,2018)。然而却很少有研究使用粒子方法研究砰击问题中被困空气的缓冲效应。Lind et al.(2015) 提出一种不可压-可压 SPH 模型，用以预测平板与不同坡度波浪砰击的砰击压力峰值。在他们的模型中，空气使用弱可压 SPH(WCSPH) 方法求解，而水使用不可压 SPH 方法 (ISPH) 求解。Khayyer and Gotoh(2016) 提出另一种基于基于投影的粒子方法的可压缩-不可压缩多相模型，用以预测砰击载荷。这个方法可被视为移动粒子半隐式方法 (MPS) 的扩展版本，并且他们的数值结果和实验数据呈现出良好的一致性。此外，Marrone et al.(2018) 研究了小静升角的平板砰击压力，并讨论了包括大水平速度分量在内的飞机水面迫降问题。

Although these numerical methods can observe intuitive fluid flows and can predict the impact pressure, considering the extreme cases of the slamming problem, the numerical simulation also faces some great challenges in accurately predicting the impact pressure. To analyze these tough slamming problems, considering the advantage of the Riemann solver to the problems of discontinuities, a multiphase Riemann SPH method is applied in the present work. In order to reduce the excessive numerical dissipation induced by the Riemann solver, a dissipation limiter for the PVRS Riemann solver is given. Owing to the usage of the Riemann solver, the present SPH method can deal with the present slamming problems with large discontinuities well, and the adopted PVRS approximate Riemann solver can better handle the problem with large density ratios. Besides, Riemann-SPH makes the stability constraint less severe and allows to set a water speed of sound able to fulfil the weakly compressible constraint (Hammani et al., 2020). For the correct simulation of the air cushion effect during water impact, the importance of using the real gas speed of sound was underlined as early as in Colagrossi and Landrini (2003). Taking this into consideration, the present SPH based on the Riemann solver uses the physical air sound speed to simulate the present problem. To maintain the uniform particle distribution and thus improving the numerical accuracy, the particle shifting technique is adopted. To verify the accuracy and the convergence of the adopted multiphase SPH method, a water slamming of a flat plate is simulated. Further, the influences of the air-cushion effect and the plate length on the slamming load are discussed. Moreover, a complex engineering problem, i.e., the slamming of the LNG tank insulation panel is simulated, and the influences of the impact velocity and deadrise angle on slamming load characteristics are analyzed.

尽管这些数值方法可以观察直观的流体流动并且能够预测砰击压力，但是考虑到砰击问题的极端情况，这些数值方法在精确预测砰击载荷方面也面临着一些极大的挑战。为了研究分析这些棘手的砰击问题，考虑到黎曼求解器求解非连续性问题的优势，本文采用多相黎曼 SPH 方法。为了减少由黎曼求解器引起的数值耗散，给出了 PVRS 黎曼求解器的耗散限制器。由于使用了黎曼求解器，当前的 SPH 方法可以很好地处理大间断的砰击问题，同时采用的 RVRS 近似黎曼求解器能够更好地处理大密度比问题。除此之外，黎曼-SPH 方法使得稳定性约束不那么苛刻，同时允许设置能够满足弱可压约束的水声速 (Hammani et al., 2020)。为了正确模拟水击过程中的气垫效应，早在 Colagrossi 和 Landrini(2003) 就强调了真实气体中的声速的重要性。考虑到这一点，当前基于黎曼求解器的 SPH 方法使用了物理空气声速模拟当前问题。为了保持粒子分布均匀并提高数值精度，本文采用了粒子转移技术。为验证采用的多相 SPH 方法的精度和收敛性，对平板水击进行了模拟。进一步讨论了气垫效应和板长对于砰击载荷的影响。此外，对一个复杂的工程问题，即 LNG 船绝缘板的砰击模拟，并分析了砰击速度和静升角度对砰击载荷特性的影响。

The paper is structured as follows: firstly, the adopted SPH method is introduced in Section 2. Then in Section 3, through the test of water slamming of the plate, the accuracy and convergence of the adopted method are validated, and the influences of the air cushion and the plate length on the slamming load are discussed. Subsequently, the slamming of the LNG tank insulation panel is simulated, and the influences of the impact velocity and deadrise angle on slamming load characteristics are analyzed. At last, some conclusions are enclosed in Section 4.

本文的结构如下：首先在第二节介绍了采用的 SPH 方法。在第三节通过板的水击试验，对采用方法的精确性和收敛性进行了验证，并讨论了气垫和板长对砰击载荷的影响。随后，对 LNG 船的绝缘板砰击进行模拟，并分析了砰击速度和静升角度对砰击载荷特性的影响。最后，在第 4 节中给出了一些结论。

3 Multiphase Riemann SPH model-多相黎曼求解器

3.1 Governing equations-控制方程

In the SPH scheme, the fluid dynamics are usually solved by the Navier–Stokes equation. For the weakly-compressible fluid, the discretized governing equations (Sun et al., 2018) in SPH method are usually written as follows

在 SPH 方法中，通常用 Navier-Stokes 方程对流体动力学进行求解。对于弱可压流体，SPH 方法中的离散控制方程 (Sun et al., 2018) 通常写作如下形式

$$\begin{cases} \frac{D\rho_a}{Dt} = -\rho_a \sum_b (\mathbf{u}_b - \mathbf{u}_a) \nabla_a W_{ab} V_b, \\ \frac{D\mathbf{u}_a}{Dt} = \mathbf{g} - \sum_b \left(\frac{\rho_a + \rho_b}{\rho_a}\right) \nabla_a W_{ab} V_b \end{cases} \quad (1)$$

in which the subscript a denotes the a-th particle, and subscript b represents the particles in the support region of particle a. The variables ρ , \mathbf{v} , V , \mathbf{g} and p refer to the density, velocity, volume, gravitational acceleration and pressure, respectively. $W(|\mathbf{r}_a - \mathbf{r}_b|, h)$ is the kernel function, in which the vector \mathbf{r} denotes the particle coordinate, and h represents the smoothing length.

式中, 下标 a 表示第 a 个粒子, 下标 b 表示在粒子 a 的支持域内的粒子。变量 ρ , \mathbf{v} , V , \mathbf{g} and p 分别代表密度, 速度, 体积, 重力加速度和压力。 $W(|\mathbf{r}_a - \mathbf{r}_b|, h)$ 是核函数, 其中向量 \mathbf{r} 表示粒子的坐标, h 表示光滑长度。

In the Riemann SPH method, every particle pair is regarded as a onedimensional Riemann problem, and the solution to every onedimensional Riemann problem can be obtained by the Riemann solver. In this way, the numerical solution of the whole field can be obtained. Specifically, particles b and a respectively carry the state of left S1 and the state of right S2, and the variables of the two states (Toro, 2013) can be written as follows

在黎曼 SPH 方法中, 每个粒子对都被视为一维的黎曼问题, 并且每个一维黎曼问题的解都可以通过黎曼求解器得到。通过这个方法, 我们可以得到整个流场的数值解。具体来说, 粒子 b 和粒子 a 分别携带了左 S1 状态和右 S2 状态, 其中两种状态的变量可以写成以下形式

$$\begin{cases} S1 : (\rho_L, u_L, p_L) = (\rho_b, \mathbf{u}_b \cdot \hat{\mathbf{r}}_{ab}, p_b), \\ S2 : (\rho_R, u_R, p_R) = (\rho_a, \mathbf{u}_a \cdot \hat{\mathbf{r}}_{ab}, p_a) \end{cases} \quad (2)$$

in which the subscripts L and R refer to the states of left and right, respectively. These two states represent expansion or shock waves, and the solution to the Riemann problem consists of two star regions which are denoted by the intermediate variables ρ_L^*, u_L^*, p_L^* and ρ_R^*, u_R^*, p_R^* , respectively. For these variables, the conditions of $u_L^* = u_R^* = u^*$ and $p_L^* = p_R^* = p^*$ need to be satisfied. Considering the approximations of $\mathbf{u}_a + \mathbf{u}_b \approx 2\mathbf{u}^*$ and $p_a + p_b \approx 2p^*$, the discrete form of governing equations (Toro, 2013) can be rewritten as follows:

式中, 下标 L 和 R 分别代表左边的状态和右边的状态。这两种状态代表膨胀波或者冲击波, 黎曼问题的解由两个星型区域组成, 分别用中间变量 ρ_L^*, u_L^*, p_L^* 和 ρ_R^*, u_R^*, p_R^* 表示。对于这些变量, 需要满足 $u_L^* = u_R^* = u^*$ 和 $p_L^* = p_R^* = p^*$ 这两个条件。考虑到 $\mathbf{u}_a + \mathbf{u}_b \approx 2\mathbf{u}^*$ and $p_a + p_b \approx 2p^*$ 的近似条件, 控制方程的离散形式可以写出以下形式

$$\begin{cases} \frac{D\rho_a}{Dt} = -2\rho_a \sum_b (\mathbf{u}^* - \mathbf{u}_a) \nabla_a W_{ab} V_b, \\ \frac{D\mathbf{u}_a}{Dt} = \mathbf{g} - 2 \sum_b \left(\frac{p^*}{\rho_a} \right) \nabla_a W_{ab} V_b \end{cases} \quad (3)$$

in which \mathbf{u}^* is computed by $\mathbf{u}^* = \mathbf{u}^* \hat{\mathbf{r}}_{ab} + [\frac{\mathbf{u}_a + \mathbf{u}_b}{2} - \frac{(u_L + u_R) \hat{\mathbf{r}}_{ab}}{2}]$, and the unit vector \mathbf{r}_{ab} is defined as $\mathbf{r}_{ab} = \frac{\mathbf{r}_a - \mathbf{r}_b}{|\mathbf{r}_a - \mathbf{r}_b|}$. p^* and u^* are intermediate variables which are solved by approximated Riemann solvers. In this work, the PVRS approximate Riemann solver (Toro, 2013) is adopted. This Riemann solver

determines the intermediate variables u^* and p^* by considering the fluid impedance, and therefore, it is suitable for handling the problem with a large density ratio. For the adopted PVRS approximate Riemann solver, u^* and p^* (Toro, 2013) are solved by

式中, $\mathbf{u}^* = \mathbf{u}^* \hat{r}_{ab} + [\frac{\mathbf{u}_a + \mathbf{u}_b}{2} - \frac{(u_L + u_R) \hat{r}_{ab}}{2}]$ 计算, 单位向量 \mathbf{r}_{ab} 定义为 $\mathbf{r}_{ab} = \frac{\mathbf{r}_a - \mathbf{r}_b}{|\mathbf{r}_a - \mathbf{r}_b|}$. p^* 和 u^* 是由近似黎曼求解器求解的中间变量。本文采用 PVRS 近似黎曼求解器 (Toro, 2013)。这个黎曼求解器通过考虑流体阻抗来确定中间变量 u^* 和 p^* , 因此该方法适合处理大密度比问题。对于采用的 PVRS 近似黎曼求解器, u^* 和 p^* (Toro, 2013) 采用下式求解

$$\begin{cases} u^* = \frac{1}{Z_L + Z_R} [Z_L u_L + Z_R u_R + (p_L - p_R)], \\ p^* = \frac{1}{Z_L + Z_R} [Z_R p_L + Z_L p_R + Z_L Z_R (u_L - u_R)] \end{cases} \quad (4)$$

in which $(\rho_L, \mathbf{u}_L, p_L, c_L) = (\rho_b, \mathbf{u}_b \cdot \hat{x}_{ab}, p_b, c_b)$ and $(\rho_R, \mathbf{u}_R, p_R, c_R) = (\rho_a, \mathbf{u}_a \cdot \hat{x}_{ab}, p_a, c_a)$, and Z_L and Z_R represent $\rho_b c_b$ and $\rho_a c_a$, respectively. c denotes the speed of sound.

式中, $(\rho_L, \mathbf{u}_L, p_L, c_L) = (\rho_b, \mathbf{u}_b \cdot \hat{x}_{ab}, p_b, c_b)$ 且 $(\rho_R, \mathbf{u}_R, p_R, c_R) = (\rho_a, \mathbf{u}_a \cdot \hat{x}_{ab}, p_a, c_a)$, 同时 Z_L 和 Z_R 分别表示 $\rho_b c_b$ 和 $\rho_a c_a$ 。 c 表示声速。

To reduce the numerical dissipation led by the Riemann solver, similar to the work of Zhang et al. (2017) and Meng et al. (2020), a dissipation limiter is applied in the computation of p^* . According to the method of Meng et al. (2020) which proposed a dissipation limiter for the Roe's approximate Riemann solver, a dissipation limiter for the PVRS approximate Riemann solver is derived in this paper, and p^* is obtained as

为减少由黎曼求解器造成的数值耗散, 与 Zhang et al. (2017) 以及 Meng et al. (2020) 的工作相似, 我们在 p_* 的计算中应用了耗散限制器。根据 Meng et al. (2020) 提出 Roe 近似黎曼求解器的耗散限制器的方法, 本文对 PVRS 近似黎曼求解器的限制器进行了推导, 其中 p^* 由下式得到

$$p^* = \frac{1}{Z_L + Z_R} [Z_R p_L + Z_L p_R + \phi Z_L Z_R (u_L - u_R)], \quad (5)$$

in which the value of ϕ is determined by $\phi = \minmax[(u_L - u_R), 0], c_{RL}/D$, where $\tilde{\rho}$ is computed by $\tilde{\rho} = \frac{2\rho_L \rho_R}{\rho_L + \rho_R}$ and c_{RL} is defined as $c_{RL} = \frac{c_R \rho_R \sqrt{\rho_R} + L \rho_L \sqrt{\rho_L}}{\sqrt{\rho_L} + \sqrt{\rho_R}}$. According to the literature (Meng et al., 2020), ∇ can be derived as $\nabla = \frac{\alpha h(c_a + c_b)}{2D(u_L - u_R)|\mathbf{x}_a - \mathbf{x}_b|}$, in which $D = \frac{2Z_L Z_R}{Z_L + Z_R}$, and the value of the parameter α is set to 0.03 for all SPH simulations in this paper. In present work, the smoothing length is set to 1.2 times of the initial particle spacing, i.e. $h = 1.2\Delta x$, and the improved Gaussian kernel function (Grenier et al., 2009) is adopted. In order to integrate the above governing equations, the predictor-corrector algorithm (Wang et al., 2019b) is applied in the present SPH scheme.

式中, ϕ 的值由 $\phi = \min\max[(u_L - u_R), 0], c_{RL}/D$ 计算得到, 其中 $\tilde{\rho}$ 由 $\tilde{\rho} = \frac{2\rho_L\rho_R}{\rho_L + \rho_R}$ 得到, 而 c_{RL} 定义为 $c_{RL} = \frac{c_R\rho_R\sqrt{\rho_R} + L\rho_L\sqrt{\rho_L}}{\sqrt{\rho_L} + \sqrt{\rho_R}}$. 根据文献 (Meng et al., 2020), ∇ 可被推导为 $\nabla = \frac{\alpha h(c_a + c_b)}{2D(u_L - u_R)|\mathbf{x}_a - \mathbf{x}_b|}$, 式中 $D = \frac{2Z_L Z_R}{Z_L + Z_R}$, 而 α 的值在该文中所有的模拟中都设置为 0.03. 本文中, 光滑长度设置为 1.2 倍的初始粒子间距, 即 $h = 1.2\Delta x$, 并采用改进高斯核函数 (Grenier et al., 2009). 为了对上述控制方程进行积分, 本文的 SPH 方法采用了预测-校正算法。

3.2 State equation of fluid-流体的状态方程

To make the governing equations closed, the equation of state is added in the SPH scheme. In present work, Tait state equation (Ming et al., 2017) is adopted with the form of

为使控制方程封闭, 需要在 SPH 方法中加入状态方程。本文采用了下式形式的 Tait 状态方程

$$p = \frac{c_0^2 \rho_0}{\gamma} ((\rho/\rho_0)^\gamma - 1) \quad (6)$$

in which ρ_0 refers to the reference density and c_0 denotes the artificial sound speed. γ is the characteristic exponent which is set as 1.4 and 7 for the air and water, respectively. In this paper, the pressure cut-off model is adopted, that is, when the pressure of fluid is less than zero, it is set to zero.

式中 ρ_0 表示参考密度, c_0 表示人工声速。 γ 是特征指数, 空气和水分别设置为 1.4 和 7. 本文采用了压力截断模型, 即当流体压力小于零时将压力值设为零。

Considering the weakly-compressible SPH method is used, to ensure the variation of the fluid density is within 0.01, the speed of sound of water (Hammani et al., 2020) is determined by

考虑到使用了弱可压 SPH 方法, 为保证流体密度变化在 0.01 内, 由下式确定水声速 (Hammani et al., 2020)

$$c_0 \geq 10 \max(|\mathbf{u}_{\max}|, \sqrt{\frac{\Delta p_{\max}}{\rho_0}}) \quad (7)$$

in which for this problem of water entry, instead of the impact velocity, the estimated maximum velocity in the flow field $|\mathbf{u}_{\max}|$ is used in the calculation of the sound speed for liquid phase (Marrone et al., 2017, 2018). Thanks for the discussion in Marrone et al. (2017), for such impact problems with small dead-rise angles, the velocity of the water jet formed by the impact cannot be neglected and can be viewed as the estimated maximum velocity to determine the sound speed. Considering a reasonable proposal for the estimated jet velocity mentioned in Marrone et al. (2017), the velocity of water jet is taken as 10 times of the impact velocity, that is, $c_{water} = 100U_{impact}$ ($Ma = U_{impact}/c_{water} = 0.01$), which is considered as a good compromise for the WCSPH. In addition, in the study of the impact of a flat plate by multiphase SPH method carried out by Cheng et al. (2017), it is reported that the numerical result with $Ma = U_{impact}/c_{water} = 0.02$ is more consistent with the experimental result.

Taking the above considerations into account and after the testing, for all the simulations in this paper, the sound speed of water satisfying $Ma = U_{impact}/c_{water} = 0.015$ is adopted. Δp_{max} is the maximum pressure variation in the liquid phase. For the air phase, the physical speed of sound is taken into account.

其中,对于该入水问题,在计算液相的声速(Marrone et al., 2017,2018)时,采用流场中的最大估计速度代替砰击速度。得益于Marrone et al. (2017)的讨论,对这种小静升角度的砰击问题,砰击形成的水射流的速度不能被忽略,且可视为确定声速的最大估计速度。考虑到Marrone et al. (2017)提到的对于估计射流速度的合理建议,即 $c_{water} = 100U_{impact}(Ma = U_{impact}/c_{water} = 0.01)$,这被视为WCSPH方法的良好折中方案。此外,在由Cheng et al. (2017)提出的基于多相SPH方法的平板砰击研究中,表明了 $Ma = U_{impact}/c_{water} = 0.02$ 时的数值结果和实验结果更加吻合。平衡上述考量并经测试,本文所有的模拟中的水声速采用 $Ma = U_{impact}/c_{water} = 0.015$. Δp_{max} 是液相中最大的压力变化。对于气相,考虑了物理声速。

In present work, the time step is determined by the following CFL condition. in which c_{max} refers to the maximum fluid sound speed.

本文中,时间步由下面的CFL条件确定,式中 c_{max} 表示流体最大声速。

$$\Delta t = \frac{0.25h}{c_{max} + |\mathbf{u}_{max}|} \quad (8)$$

3.3 Treatment of fluid-structure interface-流固界面的处理

As for dealing with fluid-structure interaction problems, it is still difficult to handle the complicated moving boundaries in SPH method. For fluid particles, the compact region truncation caused by outer boundaries leads to the error of the particle approximation and loses the accuracy of numerical results. Therefore, for SPH method, a lot of work has been carried out on the treatment of solid boundary (Adami et al., 2012; Shao et al., 2012; Leffe et al., 2009; Monaghan and Kajtar, 2009). The treatment on solid boundary in SPH method can be roughly divided into two sorts; one is to arrange one layer of particles as the solid wall boundary, in which the repulsive force is introduced to prevent the penetration of fluid particles. The other one is to set the multi-layer particles as the solid wall boundary to guarantee the integrity of the compact region. In this work, the wall boundary condition developed by Adami et al. (2012), whose accuracy and robustness have been proved by many works, is applied. In this boundary condition, the multi-layer dummy particles are placed, which can ensure that for the fluid particles, the particle approximations can be conducted by enough particles in the compact region. In addition, dummy particles are viewed as fluid particles to participate in the information update (e.g. density, velocity, etc.) of other fluid particles. For dummy particles (Adami et al., 2012), the pressure is obtained by interpolating from fluid particles in the compact region as follows:

至于处理流固耦合问题,SPH方法依然很难处理复杂的运动边界。对于弱可压流体粒子,由与外部边界导致的紧支域截断会产生粒子近似的误差和数值结果精度的丢失。因此,对于SPH方理固体边

界的处理 (Adami et al., 2012; Shao et al., 2012; Leffe et al., 2009; Monaghan and Kajtar, 2009), 已经开展了大量的工作。SPH 方法中的固体边界的处理可以大致分为两类；一类是布置一层粒子作为固体壁面边界，并引入排斥力以防止流体粒子的穿透。另一类是设置多层粒子作为固体壁面边界以保证紧支域的完整性。本文采用了 Adami et al. (2012) 提出的固体壁面边界条件，大量工作证明了其精确性和鲁棒性。在这种边界条件下，放置了多层虚拟粒子，确保对于流体粒子的紧支域内有足够的粒子进行粒子近似。此外，虚拟粒子被视为流体粒子，参与其他粒子的信息更新(如密度，速度等)。对于虚拟粒子 (Adami et al., 2012)，压力由紧支域内的流体粒子插值得到，如下：

$$p_d = \frac{\sum_f p_f W_{df} + \sum_f \rho_f (\mathbf{r}_f - \mathbf{r}_d)(\mathbf{a}_d - \mathbf{g})W_{df}}{\sum_f W_{df}}, \quad (9)$$

in which the subscript d represents the dummy particle, and f denotes the fluid particle. \mathbf{a}_d is the acceleration of dummy particles. Based on the pressure of the dummy particle, its density (Adami et al., 2012) can be obtained according to the equation of state as

式中下标 d 表示虚拟粒子，f 表示流体粒子。 \mathbf{a}_d 是虚拟粒子的加速度。基于虚拟粒子的压力，可以通过下式形式的状态方程得到其密度：

$$\rho_d = \rho_0 \left(\frac{p_b \gamma}{c_0^2 \rho_0} + 1 \right)^{\frac{1}{\gamma}} \quad (10)$$

For the fixed wall boundary particles, their velocity and acceleration are zero, while for the moving rigid body particles in this work, the velocity and acceleration of these particles can be updated by the following equations (Sun et al., 2018), in which the subscript w refers to the moving rigid body particle.

对于固定壁面边界粒子，其速度和加速度为零，然而本文中的运动刚体粒子的速度和加速度可使用下面的方程 (Sun et al., 2018) 更新，式中下标 w 表示运动缸体粒子。

$$\begin{cases} \mathbf{u}_w = \mathbf{U}_0 + \omega_0 \times \mathbf{r}_{w0}, \\ \mathbf{a}_w = \frac{D\mathbf{U}_0}{Dt} + \frac{D\omega_0}{Dt} \times \mathbf{r}_{w0} + \omega_0 \times \mathbf{u}_{w0} \end{cases} \quad (11)$$

in which \mathbf{r}_{w0} and \mathbf{u}_{w0} can be calculated by $\mathbf{r}_{w0} = \mathbf{r}_w - \mathbf{r}_0$ and $\mathbf{u}_{w0} = \mathbf{u}_w - \mathbf{U}_0$, respectively. \mathbf{U}_0 and ω_0 represent the translational and rotational velocities of the mass center of the rigid body, respectively, and their values (Sun et al., 2018) are obtained by

式中 \mathbf{r}_{w0} 和 \mathbf{u}_{w0} 可以分别通过 $\mathbf{r}_{w0} = \mathbf{r}_w - \mathbf{r}_0$ 和 $\mathbf{u}_{w0} = \mathbf{u}_w - \mathbf{U}_0$ 计算， \mathbf{U}_0 和 ω_0 分别代表质心的平移和转动，它们的值 (Sun et al., 2018) 可以通过下式计算得到

$$\begin{cases} \frac{D\mathbf{U}_0}{Dt} = \frac{F_{fw}}{M} + \mathbf{g}, \\ \frac{D\omega_0}{Dt} = \frac{\mathbf{T}_{fw}}{I} \end{cases} \quad (12)$$

in which \mathbf{M} and \mathbf{I} denote the mass and the moment of inertia of the moving rigid body, respectively. F_{fw} and T_{fw} (Sun et al., 2018) can be calculated as follows:

式中 \mathbf{M} 和 \mathbf{I} 分别代表运动刚体的质量和动量。 F_{fw} 和 T_{fw} (Sun et al.,2018) 可以通过下式计算：

$$\begin{cases} \mathbf{F}_{fw} = \sum_f \sum_w \left(\frac{\mathbf{r}_f + \mathbf{r}_w}{2} - \mathbf{r}_c \right) \times p_{fw} (V_f^2 + V_w^2) \Delta_f W_{fw}, \\ p_{fw} = \frac{\rho_w p_f + \rho_f p_w}{\rho_f + \rho_w} \end{cases} \quad (13)$$

where p_{fw} is computed by $p_{fw} = \frac{\rho_w p_f + \rho_f p_w}{\rho_f + \rho_w}$, and $matbfr_c$ is the centroid position of the rigid body.

式中 p_{fw} 通过 $p_{fw} = \frac{\rho_w p_f + \rho_f p_w}{\rho_f + \rho_w}$ 计算， \mathbf{r}_c 是刚体的质心。

3.4 Particle shifting technique(PST)-粒子转移技术

For the SPH method, maintaining the regularity of particle distribution is helpful to improving the accuracy of the numerical results. Therefore, many papers focus on maintaining even particle distributions in simulations (see e.g. Lind et al., 2012; Xu et al., 2009; Khayyer et al., 2017, 2019; Sun et al., 2017; Wang et al., 2019c). To ensure that particle shifting will be conducted in a physically-consistent manner (i.e., no unphysical shifting at the interface), multiphase shifting schemes need to be considered. To our best knowledge, Mokos et al. (2017) was the first to extend PST to multiphase SPH method, and recently Khayyer et al. (2019) has further developed PST into the projection-based particle method. Considering the applied WCSPH method, the particle shifting formulation in Mokos et al. (2017) is adopted and then combined with the multiphase interface treatment of Khayyer et al. (2019) in the present simulation. To be specific, the shifting displacement vector of particle based on the magnitude of particle velocity (Mokos et al., 2017) can be described as:

对于 SPH 方法，保持粒子分布的均匀性有利于提高数值结果的精度。因此很多文献专注于在模拟中保持均匀的粒子分布 (见如 Lind et al.,2012;Xu et al.,2009;Khayyer et al.,2017, 2019;Sun et al.,2017;Wang et al.,2019c)。为了保证粒子转移以符合物理规律地方式进行，需要考虑多相转移方法。据我们所知，Mokos et al. (2017) 首次将 PST 扩展到多相 SPH 方法中，而 Khayyer et al. (2019) 最近进一步将 PST 改进到基于投影的粒子方法中。鉴于采用了 WCSPH 方法，本文中的模拟采用了 Mokos et al.(2017) 中的粒子位移公式，并结合 Khayyer et al.(2019) 的多相界面处理手段。具体而言，粒子基于粒子速度大小的位移向量 (Mokos et al.,2017) 可以由下式描述：

$$\delta \mathbf{r}'_a = -A_s h |\mathbf{u}|_{max} \Delta t \nabla C_a; \nabla C_a = \sum_b \nabla_a W_{ab} V_b, \quad (14)$$

in which the parameter A_s is set to 2 (Skillen et al., 2013). $|\mathbf{u}|_{max}$ denotes the maximum particle velocity and Δt represents the time step. Besides, the treatment of the multiphase particle shifting technique developed by Khayyer et al. (2019) is applied, which mainly consists of two steps. Firstly, the particles of heavy phase are shifted by neglecting the particles of light phase, which indicates that

the water-gas interface can be regarded as the free surface. The shifting of the heavy phase particles (Khayyer et al., 2019) is as follows

式中参数 A_s 设为 $2|\mathbf{u}|_{max}$ 表示最大的粒子速度 Δt 表示时间步。此外, 采用了 Khayyer et al.(2019) 发展的多相粒子转移技术, 其主要包含两个步骤。首先忽略轻相粒子, 重相粒子移动, 这表明气液界面可被视为自由表面。重相粒子的移动描述如下

$$\delta\mathbf{r}_a = \begin{cases} 0, & \text{if } a \in A_1, \\ (\mathbf{I}_{\tilde{n}_a} \otimes \tilde{n}_a) \delta\mathbf{r}_a & \text{if } a \in A_2, \\ \delta\mathbf{r}'_a & \text{if } a \in A_3 \end{cases} \quad (15)$$

in which \mathbf{I} is the identity tensor and \tilde{n}_a is the modified normal unit vector of the surface (Khayyer et al., 2019), which is computed by

式中 \mathbf{I} 是身份张量, \tilde{n}_a 是修正法向单位向量 (Khayyer et al., 2019), 其可由下式计算

$$\tilde{n}_a = -\frac{\mathbf{B}_a \cdot \Delta C_a}{|\mathbf{B}_a \cdot \Delta C_a|}; \mathbf{B}_a = \left(\sum_b \mathbf{r}_{ab} \otimes \Delta_a W_{ab} V_b \right)^{-1}, \quad (16)$$

A_1 denotes the splashing particles, A_2 represents the free surface particles but excluding splashing particles, and A_3 refers to the interior heavy phase particles. For the assessment of the particle type, the optimized free surface detection method introduced by Wang et al. (2019c) is adopted, in which the free surface particles are roughly detected according to the divergence of the position vector (Lee et al., 2008), and then through scanning the “umbrella-shaped” area introduced in Marrone et al. (2010), the free surface particles are further distinguished.

A_1 表示溅起的粒子, A_2 表示不包含溅起的粒子的自由表面粒子, A_3 表示内部重相粒子。对于粒子类型的判断, 本文采用了 Wang et al. (2019c) 提出的优化自由表面搜索法, 其通过位置矢量的散度 (Lee et al., 2008) 对自由表面的粒子进行大致搜索, 随后 Marrone et al. (2010) 提出的通过伞状区域进行扫描对自由表面粒子进一步区分。

After conducting the shifting of the heavy phase particles, the particles of light phase are shifted, and at this time the regularized particles of heavy phase need to be considered. The shifting of light particles can be calculated by

在重相粒子移动完成后, 轻相粒子移动, 并且此时需要考虑重相正则化的粒子。轻相粒子的移动可以通过下式计算

$$\delta\mathbf{r}_a = \delta\mathbf{r}'_a \quad (17)$$

It can be observed that different from the shifting of water particles, the air particles can be shifted freely in all directions, which aims to eliminate the voids appearing in air during simulations.

可以观察到，与水颗粒的移动不同，空气颗粒可以在各个方向自由移动，其目的是消除模拟过程中空气中出现的空隙。

4 Numerical result and discussion-数值结果和讨论

In this section, firstly, the accuracy and convergence of the adopted multiphase Riemann-SPH method are validated through the test of the slamming of a flat plate. Then, the influences of the air cushion and the plate length on the slamming load are discussed. Finally, focusing on the air-cushion effect in the water entry, a complex engineering problem, i. e., the slamming of the LNG tank insulation panel is simulated, and the influences of the impact velocity and deadrise angle on slamming load characteristics are analyzed.

本节通过平板砰击实验验证了采用的黎曼-SPH 方法的精确性和收敛性。随后，讨论了气垫效应和板长对砰击载荷的影响。最后，重点研究了入水过程中的气垫效应，模拟了一个复杂的工程问题，即 LNG 船绝缘板的砰击，并分析了砰击速度和静升角对砰击载荷特性的影响。

4.1 slamming of flat plate-平板砰击

4.1.1 Validation-验证

This subsection aims to verify the accuracy and convergence of the adopted SPH method by the test of water slamming of flat plate which is carried out by Ma et al. (2016). The sketch of the numerical model is shown in Fig. 1, in which M , l and U_{impact} stand for the mass, the length and the impact velocity of the plate, respectively. H and W denote the depth and width of water domain, respectively. In the experiment, the plate has the length of $l = 0.25m$ and the mass of $M = 32kg$. This plate is released at rest initially and falls freely, and it impacts the water at the velocity of $5.5m/s$. In our simulation, the width and depth of the water domain are set to $W = 1.2m$ and $H = 0.4m$, respectively. In addition, the reference density of water and air is set to $1000kg/m^3$ and $1kg/m^3$, respectively, and the particle spacing Δx is set to $0.002 m$. In literature (Ma et al., 2016), the moment when the plate impacts the water is defined as the origin of the time coordinate. For easy to compare, the time coordinate of the numerical results is translated to make it consistent with that of the literature (Ma et al., 2016).

这一小节旨在通过由 Ma et al.(2016) 提出的平板砰击实验验证所采用的 SPH 方法的精确性和收敛性。数值方法的示意图如 Fig.1 所示，其中 M, l, U_{impact} 分别表示板的质量，长度和砰击速度。 H 和 W 分别表示水域的深度和长度。在实验中，板长 $l = 0.25m$ ，板的质量为 $M = 32kg$. 板由静止释放并自由下落，最后以 $5.5m/s$ 的速度与水砰击。在本文的数值模拟中，水域的宽度和深度分别设置为 $W = 1.2m$ 和 $H = 0.4m$. 此外，水和空气的参考密度分别设置为 $1000kg/m^3$ 和 $1kg/m^3$ ，粒子的间距 Δx 设置为 $0.002m$. 在文献 (Ma et al.,2016)，平板刚与水砰击的时刻定义为时间坐标的原点。为了便

于对比，对本文数值结果的时间坐标平移，使之与文献 (Ma et al.,2016) 一致。

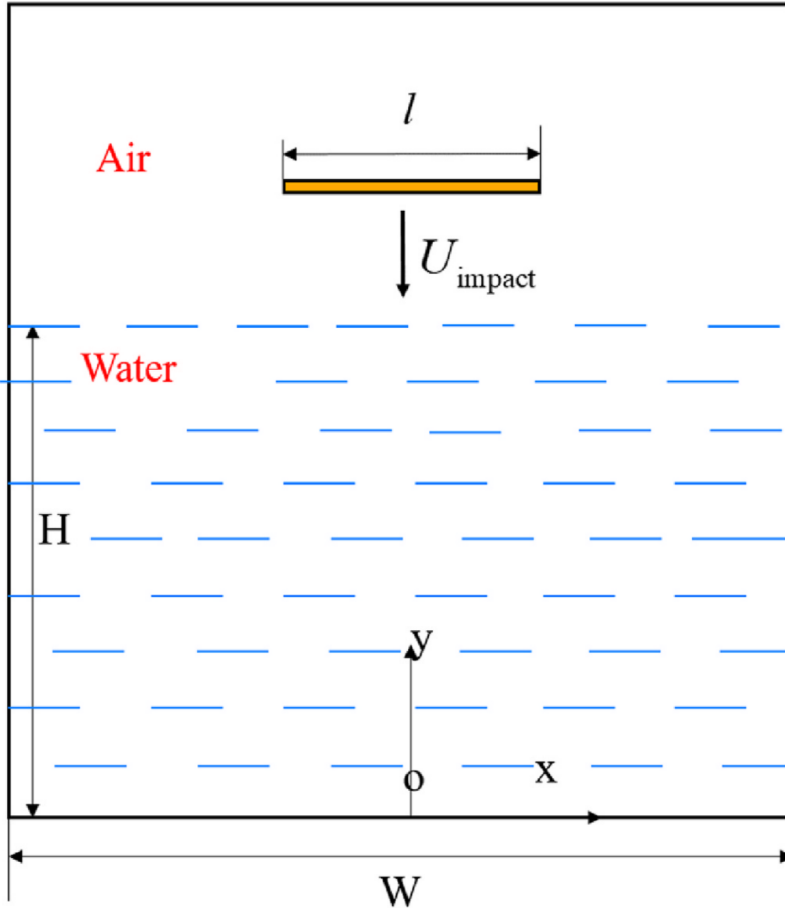


Fig. 1. Sketch of the water slamming of a flat plate.

From the velocity field shown in Fig. 2, it can be observed that clear circulating air jet surrounding the plate is generated during the falling process. This is because the air under the plate is compressed during the falling of the plate, causing the pressure of the air under the plate to increase and the pressure of the air above the plate to decrease. As a result, the air flows around the edges of the plate, which in turn forms a circulating air vortex as displayed in Fig. 2. When the plate is about to contact with the water, the velocity of the air escaping from both sides is very large even over $100m/s$, although the impact velocity of the plate is only $5.5m/s$ in this case. Similar situation can be found in the research of Lind et al. (2015) in which it is believed that the high-speed subsonic flow is readily formed for the air in the water slamming of plate even in a moderate impact event. During the impact of plate, a part of air is trapped under the plate and forms the air cushion for the slam plate, as shown in Fig. 3. At the same time, the pressure distribution of the slam plate is displayed. Aiming at the numerical prediction of the slamming load of the plate, the time histories of the pressure of the plate center and the slamming force of the whole plate are given in Fig. 4 and Fig. 5, respectively. It can be found that generally, the time history of the pressure at the center of plate obtained by adopted the present

SPH method agrees well with the FVM result provided by Ma et al. (2016) but a little lower than the experimental data in (Ma et al., 2016). For the slamming force of the whole plate, the present result obtains a higher peak compared with the SPH result of Yang et al. (2020), and the result obtained by present SPH method shows good agreement with the results of experiment and FVM method in Ma et al. (2016). In general, for the present test of the water slamming of flat plate involving air-cushion effect, the present method has good accuracy in predicting the slamming load of structure.

从速度场如 Fig. 2, 可以明显看出在下落过程中板周围产生了环状空气射流。这是因为板下空气在下落过程中被压缩, 导致板下空气压力升高而板上空气压力下降。因此, 空气绕过平板边缘流动, 进而形成如 Fig. 2 所示的环状空气漩涡。尽管此时板的砰击速度只有 5.5m/s 当平板即将接触水面时, 从板端逸出的空气速度非常大, 甚至超过 100m/s . 类似的情况可以在 Lind et al. (2015) 的研究中发现, 他认为对于空气而言在板与水的砰击过程中, 即使在缓和的砰击情况下高速亚音速流也会快速形成。在板的砰击过程中, 一部分空气困在板下并为砰击板形成缓冲, 如 Fig. 3 所示。同时压力分布也如图所示。针对板的砰击载荷的预测, 板中心压力的时间历程和整个板的砰击力分别由 Fig. 4 和 Fig. 5 给出。结果表明, 由本文采用的 SPH 方法获得的板中心压力时间历程和由 Ma et al. (2016) 获得的 FVM 结果吻合的很好, 但略低于 (Ma et al., 2016) 的实验数据。至于整个板的砰击力, 本文的结果比 Yang et al. (2020) 的 SPH 结果的峰值更高, 但本文 SPH 方法获得的结果和实验结果以及 Ma et al.(2016) 有很好的一致性。总而言之, 对于包含气垫效应的平板和水的砰击实验, 当前本文的方法表现出良好的结构物砰击载荷的预测精度。

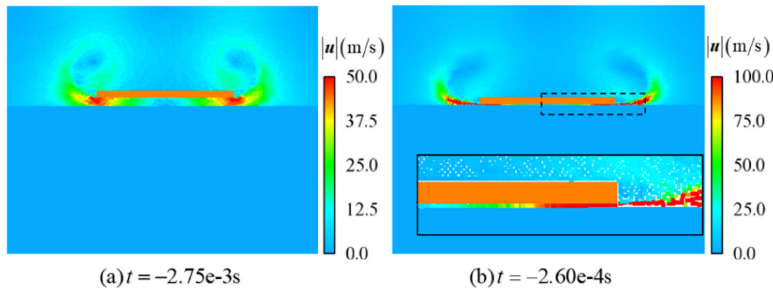


Fig. 2. The velocity field of the air surrounding the falling plate.

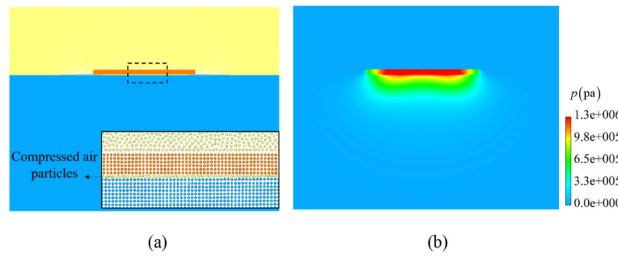


Fig. 3. (a) Particle distribution of the slam plate in the pre-impact at $t = -2.60\text{e}-4\text{s}$ (b) Pressure distribution of the impact at $t = 0 \text{ s}$.

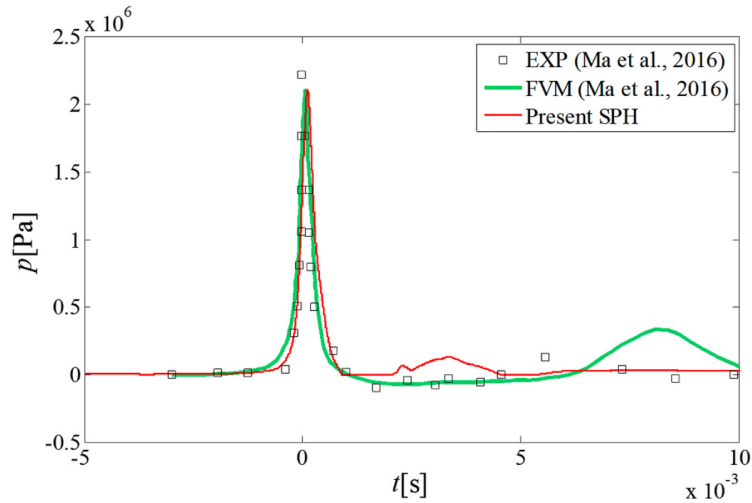


Fig. 4. Time histories of the pressure at the plate center compared with the experimental result (Ma et al., 2016) and FVM result in (Ma et al., 2016).

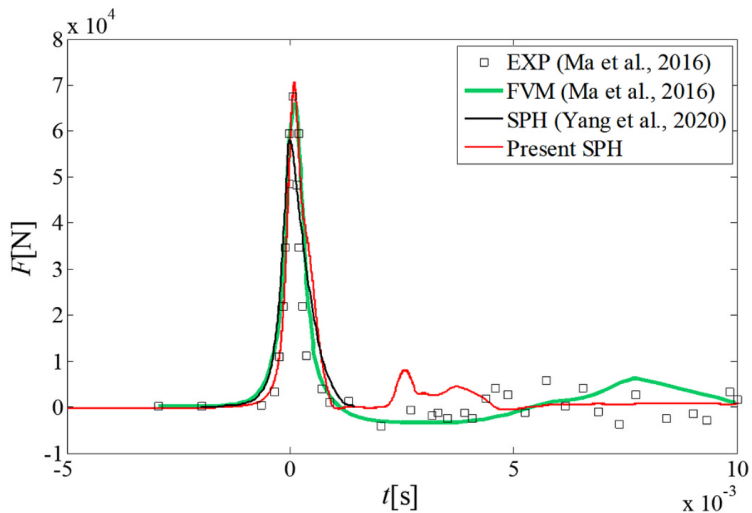


Fig. 5. Time histories of the slamming force of plate compared with the experimental result (Ma et al., 2016), the FVM result (Ma et al., 2016) and the SPH result of Yang et al. (2020).

Furthermore, also through this numerical test, the convergence property of the adopted SPH model is checked. Here, the simulations with the particle resolutions of $\Delta x = 0.003\text{m}$ and $\Delta x = 0.0015\text{m}$ are performed, respectively. Combined with the numerical results with $\Delta x = 0.002\text{m}$, the time histories of the pressure at the plate center and the slamming force of whole plate with three different particle resolutions are displayed in Fig. 6. It can be found that similar results of the pressure at the plate center and the slamming load of plate are obtained with the particle resolution increasing from $\Delta x = 0.002\text{m}$ to $\Delta x = 0.0015\text{m}$, which indicates that the adopted SPH scheme has a good convergence.

此外，此次数值试验验证了采用的 SPH 方法的收敛性质。这里分别进行了粒子分辨率为 $\Delta x = 0.003m$ 和 $\Delta x = 0.0015m$ 的模拟。结合 $\Delta x = 0.002m$ 的数值结果，不同粒子分辨率的板中心压力的时间历程和整个板的砰击压力如 Fig. 6 所示。可以发现粒子分辨率从 $\Delta x = 0.002m$ 增加的 $\Delta x = 0.0015m$ 时，板中心压力的时间历程和整个板的砰击力有类似的数值结果，这表明本文采用的 SPH 方法有良好的收敛性。

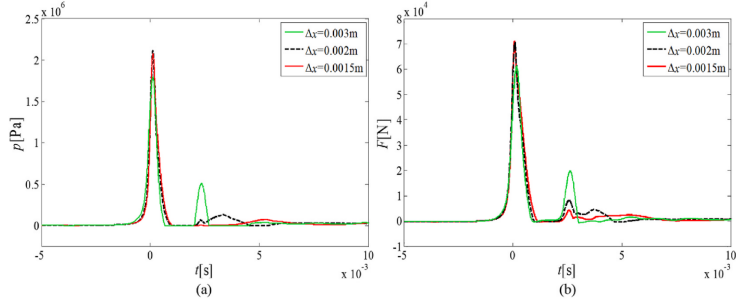


Fig. 6. Time histories of the pressure at the plate center (left) and the slamming force of plate (right) with three particle resolutions.

4.1.2 Influence of the air on slamming load of flat plate-空气对砰击载荷的影响

To investigate the effect of the air on the water impact of the flat plate, the slamming loads of the plate obtained by taking the air into account or not are compared. Fig. 7 shows the pressure distributions at $t = 0s$ of the computational domain in the presence and absence of air, respectively. It can be seen that owing to the existence of the air under the plate, the value of the slamming pressure of the plate is reduced substantially, and the area of the pressure surface under the plate is also reduced.

为研究空气对于平板和水砰击的效应，比较考虑和不考虑情况下的板的砰击载荷。Fig. 7 分别展示了有空气和没有空气 $t = 0s$ 时计算域内的压力分布。结果表明，由于板底空气的存在，板的砰击压力的值大幅下降，而且板底的压力面面积也有所减小。

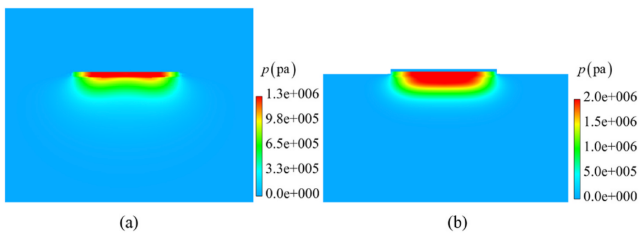


Fig. 7. (a) Pressure distribution of the slam plate with air at $t = 0s$. (b) Pressure distribution of the slam plate without air at $t = 0s$.

Fig. 8 displays the comparison of the slamming load of plate with and without air. It can be seen that ignoring the air overestimates the magnitude of the slamming load and underestimates the pulse width of the impact, which reflects the buffering effect of air cushion for the impact. In addition, due to the existence of the air, the reflection wave becomes obviously weakened in the post-impact. The reason is that the impedance of the air is much smaller than that of the water. When the reflected pressure wave propagates from the water to the air under the plate, that is, from the high-impedance medium to the low-impedance medium, the pressure wave is significantly reduced.

Fig. 8 显示了有无空气的砰击载荷的比较。可以看书忽略空气导致过高估计了砰击载荷，却过低估计了砰击的宽度，其反应了气垫的缓冲效应。此外由于空气的存在，反射波在砰击后明显减弱。因为空气的阻抗远远小于水的阻抗。当反射压力波从水中传播到板下空气中时，即从高阻抗介质到低阻抗介质，压力波显著较小。

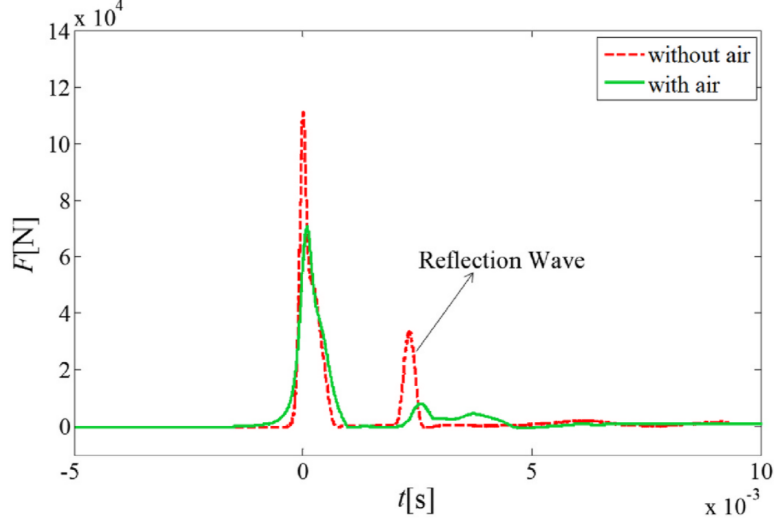


Fig. 8. Time histories of the slamming load of plate with and without air.

4.1.3 Influence of the plate length on slamming load-板长对于砰击载荷的影响

Fig. 9 shows the time histories of the slamming force of the plate with different lengths in the presence and absence of air. It can be found that the slamming force of the plate as well as the reflection pressure load increase rapidly as the plate length becomes larger. The reason accounts for this phenomenon is that a wider plate tends to result in a larger contact area and thus a larger slamming load. In addition, as shown in Fig. 9, ignoring the air obviously overestimates the slamming load of the plate, and the buffering effect of the air cushion becomes more significant with the increase of the plate length. More specifically, in terms of the moment of water slamming, the change of plate length has little influence on the contact time between the plate and water when the air is ignored. However, when the air is taken into account, it is shown that with the increase of the plate length, the occurrence time of the impact is delayed. The reason is that the larger the plate length, the greater the amount of air trapped under the plate. Therefore, under the compression effect of the air, the contact between the plate and water becomes later, leading to the lag of the peak of the slamming load. From the perspective of the magnitude of slamming load, Table 1 displays the comparison on the peaks of the slamming force of plate with different lengths in the presence and absence of air. Here, the peak values of the slamming force with and without air are defined as F_{air} and F_{noair} , respectively. Owing to the more significant cushioning effect of air under the wider plate, the difference in the peak value of the slamming force in the presence and absence of air is getting larger, as shown in Table 1. For the case with plate of $l = 0.5m$, the magnitude of the slamming force is reduced by 45.8% thanks to the existence of the air.

Fig. 9 展现了有无空气时不同板长的砰击压力的时间历程。可以发现随着板长增大，砰击载荷和反射压力载荷迅速增大。解释这一现象的原因是板长趋于越长，导致越大的接触面积，因而砰击载荷越大。此外，如 Fig. 9 所示，忽略空气会显著过高估计砰击压力，并且气垫的缓冲效应随着板长的增加变得更加显著。更具体而言，就入水砰击的时刻而言，当忽略空气时，板长的变化对空气和水的接触时刻影响很小。然而，当考虑空气时，结果表明随着板长增加，接触时刻会延后。其原因是当板长越长，困在板下的空气数目越多。因此，由于空气的压缩效应，板和水的接触变迟，导致砰击载荷峰值的滞后。从砰击载荷大小的角度看，Table 1 比较了有无空气时不同板长的平板砰击力峰值。这里有无空气的砰击力分别用 F_{air} 和 $F_{no_{air}}$ 表示。因为更宽的板下的缓冲效应更明显，有无空气的砰击力峰值的差异变得更大，如 Table 1 所示。在板长 $l = 0.5m$ 的情况下，得益于空气的存在，砰击力的大小减小了 45.8%。

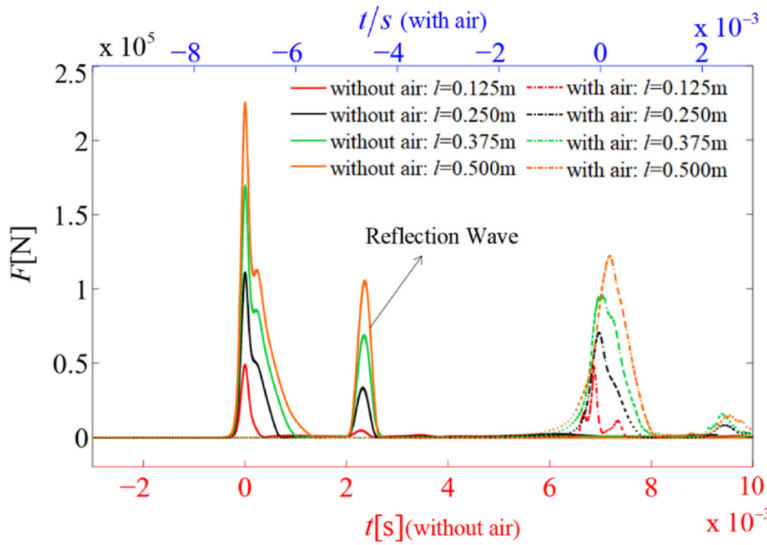


Fig. 9. Time histories of the slamming force of the plate with different lengths in the presence and absence of air.

4.2 Slamming of LNG tank insulation panel-LNG 船绝缘板砰击

4.2.1 Simulation of slamming process

In this subsection, focusing on the air-cushion effect in the water entry, a complex practical problem studied in Marrone et al. (2017), i.e., the slamming of the LNG tank insulation panel, is simulated, and the related accuracy test is provided in Appendix A. For the simulation of the slamming of LNG tank insulation panel in the present work, the computational model including the water region and the insulation panel is sketched in Fig. 10, which is similar to that in Marrone et al. (2017). In the present simulation, the mass of the insulation panel is 69.7kg, and the insulation panel impacts on the water with a vertical velocity of 5.5m/s. The particle resolution is set to $\Delta x = 0.002m$, and the whole computational domain is discretized into 312992 particles.

在本小节中，模拟了 Marrone et al. (2017) 研究的一个复杂的工程问题，即 LNG 船绝缘板的砰击，重点研究了入水过程中的气垫效应，并在附录 A 中提供相应的精度测试。对于本文的 LNG 船绝缘

板的模拟，计算模型与 Marrone et al. (2017) 类似，包括水域和绝缘板，如 Fig. 10 所示。本文的模拟中，绝缘板的质量时 $69.7Kg$ ，绝缘板的与水砰击的速度是 $5.5m/s$ 。粒子分辨率设置为 $\Delta x = 0.002m$ ，整个计算域离散为 312992 个粒子。

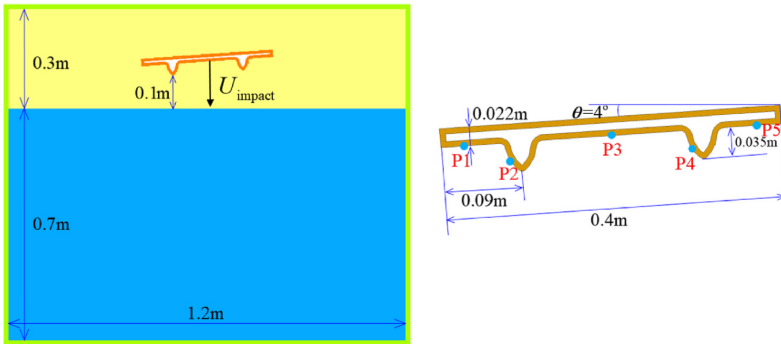


Fig. 10. Slamming of LNG tank insulation panel. Sketch of the computational model.

Fig. 11 shows the particle distributions and corresponding pressure fields at several typical time instants. It can be seen that with the fall of the panel, the left dent of the plate first touches the water surface at about $t = 0.0186s$. Subsequently, the right dent impacts on the water, and an air bubble is generated by the entrainment of the air. During $t \in (0.0207s, 0.0237s)$, as the panel continues to fall, the bubble volume decreases and thus the bubble pressure increases. It can be seen that the pressure inside the bubble is uniform and continuous across the waterair interface. At $t = 0.0237s$, the left corner of the panel impacts on the water violently, producing a large impact pressure wave. At last, the right corner of panel impacts on the water with the impact pressure peak much smaller than that produced by the impact of the left corner. During $t \in (0.0237s, 0.0282s)$, the air bubble expands and overflows from the right dent, and because of the increase of volume of the air bubble, the bubble pressure becomes lower.

Fig. 11 给出了几个典型时刻的粒子分布和相应的压力场。可以看出随着平板的下落，左齿大约在 $t = 0.0186s$ 首先接触水面。随后，右齿与水砰击，并且由于空气的卷入产生了气泡。在 $t \in (0.0207s, 0.0237s)$ 时间内，随着板持续下落，气泡的体积减小而气泡内压力上升。可以看出，气泡内部的压力在整个水气界面处是均匀且连续的。在 $t = 0.0237s$ 时，板的左角与水面猛烈砰击，产生了巨大的砰击压力波。最后，板的右角与水面砰击，其砰击压力波峰值远小于左角砰击所产生的。在 $t \in (0.0237s, 0.0282s)$ 时间内，气泡膨胀并从左齿逸出，由于气泡体积的增大，其压力开始减小。

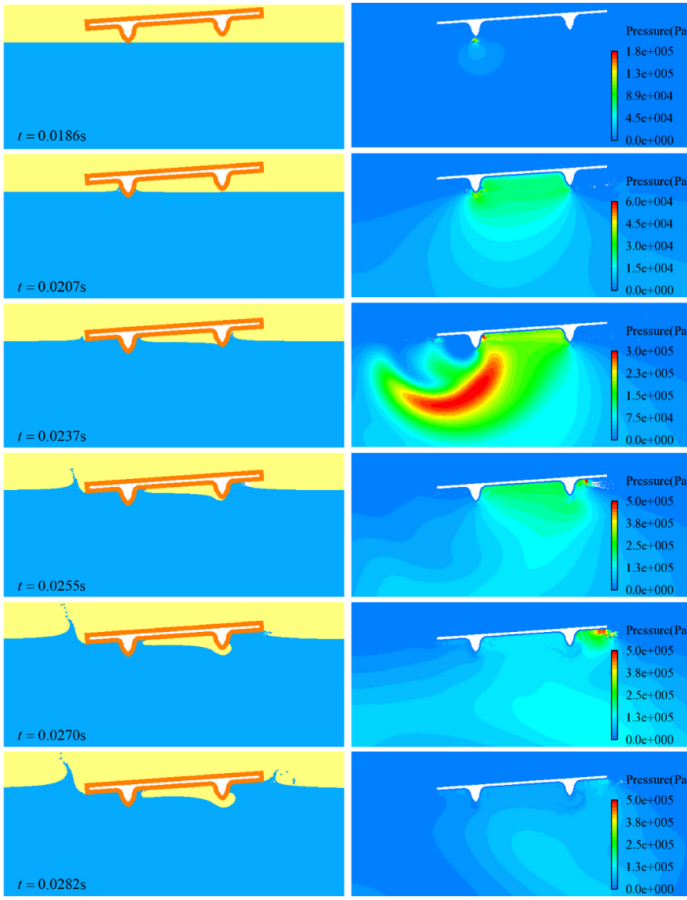


Fig. 11. Slamming of LNG tank insulation panel. Particle distributions and pressure fields at six instants.

Fig. 12 gives the time histories of the pressure of the five measuring points on the panel. It can be observed that for the point P1 which is located at the left corner of the panel, its pressure peak is the largest among all the measuring points. This large pressure load results from the slamming by the high-speed water jet generated near the left dent. For P2 which is on the left side of the left dent, although this measuring point contacts with water earliest, the pressure peak is much smaller than that of P1. The reason is that the water impact occurs at a certain angle for P2, which considerably reduces the slamming load. Different from the other measuring points, the pressure histories curves of P3 and P4 are very smooth without obvious oscillations, and their peak values are closed but much smaller than those of other measuring points. This can be explained by the fact that these two points are surrounded by the air bubble entrapped by the panel during slamming, so their pressure is approximately equal to that of the air-bubble, and the slamming load is reduced significantly due to the buffering effect of the air-cushion. For P5, its pressure peak becomes oscillatory again due to the absence of aircushion. Besides, because of the decrease of the velocity of the panel, the peak value of P5 is less than that of P1.

Fig. 12 给出了板上五个测量点压力的时间历程。可以看出板的左角的 P1 点的压力峰值是所有测量点中最大的。这个大压力载荷是由左齿附近的高速水射流碎击造成的。P2 位于左齿的左侧，尽管该

测量点最先接触水面，但是其压力峰值远小于 P1 的。原因是与水对 P2 的砰击发生在某个特定的角度，从而大幅地减小了砰击载荷。与其他测量点不同，P3 和 P4 的压力曲线非常平滑，没有明显的震荡，而且它们的峰值非常接近，但远小于其他测量点的峰值。这可以被解释为事实上这两个点被板下落过程中困住的气泡所包围，所以其压力与气泡压力近似相等，并且由于气垫的缓冲效应，砰击载荷大幅降低。对于 P5，由于气垫的消失，其压力再次出现震荡。此外，由于板的速度的下降，P5 的峰值也小于 P1.

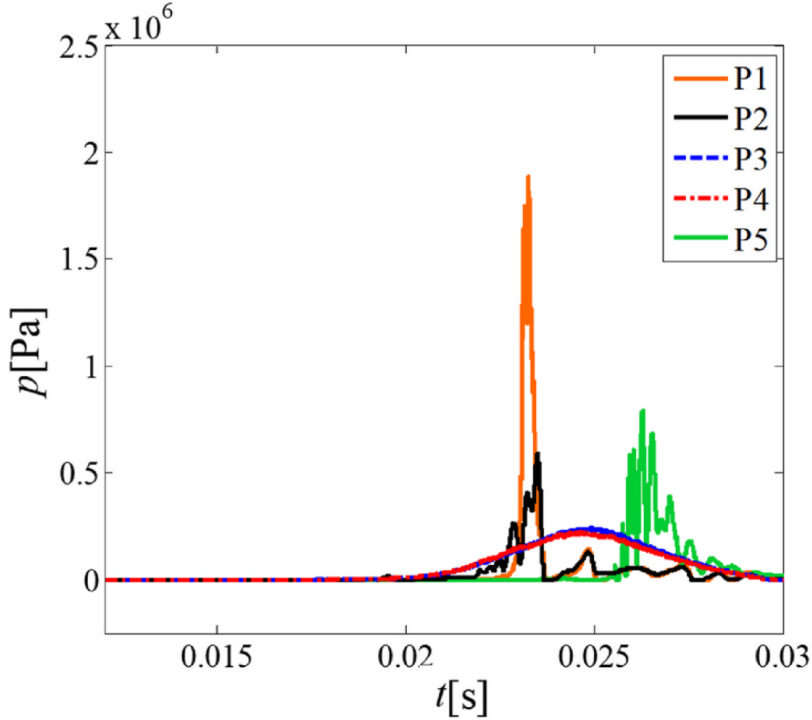


Fig. 12. Slamming of LNG tank insulation panel. Time histories of the pressure of the measuring points located on the LNG tank insulation panel.

4.2.2 Influence of the impact velocity on slamming of LNG tank insulation panel-砰击速度对于 LNG 船绝缘板砰击的影响

To investigate the effect of impact velocity on slamming pressure of LNG tank insulation panel, the simulations are conducted by adjusting the initial impact velocity to $U_{impact} = 2.5m/s$ and $U_{impact} = 4m/s$, respectively, and other conditions are same as those in subsection 3.2.1. Combined with the obtained numerical result with $U_{impact} = 5.5m/s$, the influence of impact velocity on load characteristics at different measuring points on the panel is discussed. Fig. 13 displays the particle distributions of the water slamming of LNG tank insulation panel with different impact velocities. It can be observed that when the impact velocity ranges from 2.5m/s to 5.5m/s, the evolution of the water surface and the air-cushion are similar. When the impact velocity increases, the splash caused by the slamming becomes more intense and the volume of the generated air bubble under the panel is smaller. To investigate the effect of impact velocity on the slamming load of LNG tank insulation panel, Fig. 14

gives the time histories of the pressure of the five measuring points on the panel with different impact velocities. Because the panel with lower velocity falls in air for a longer time, the pressure peak of measuring points at the panel with lower velocity appears later, but the trends of the time histories of the pressure of the measuring points are also similar. Further, for all measuring points, the slamming pressure peaks increase monotonously with the increase of slamming speed. For all the three cases with different impact velocities, the maximum slamming loads are all recorded at the measuring point P1, and the three pressure peaks are 1.88 MPa, 1.49 MPa and 0.61 MPa, respectively.

为了研究砰击速度对于 LNG 船保温杯砰击压力的影响，分别调整初始砰击速度为 $U_{impact} = 2.5m/s$ 和 $U_{impact} = 4m/s$ ，其他条件和 subsection 3.2.1 相同，并进行模拟。结合已获得的 $U_{impact} = 5.5m/s$ 数值结果，讨论了砰击速度对于不同测量点的载荷特性。Fig. 13 给出了不同速度的 LNG 船绝缘板与水砰击的粒子分布情况。可以看到砰击速度从 $2.5m/s$ 到 $5.5m/s$ ，水面和气垫的演变类似。当砰击速度增加，砰击造成的飞溅更加剧烈并且板底生成气泡的体积更小。为了研究砰击速度对于 LNG 船保温杯砰击压力的效果，Fig. 14 给出了不同砰击速度下板上五个测量点的压力时间历程。因为速度越低的板在空中下落时间更长，所以更低速度的板的压力峰值出现地更晚，但是测量点压力随时间变化的趋势相似。此外，所有测量点的压力峰值随着砰击速度的增加而单调增加。在不同砰击速度的三种情况下，最大砰击载荷都记录在测量点 P1，并且三个压力峰值分别为 $1.88MPa$, $1.49MPa$ 和 $0.61MPa$.

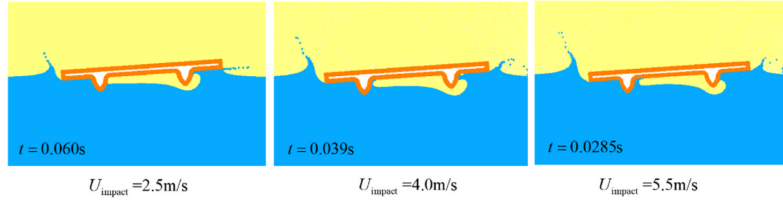


Fig. 13. Particle distributions of the water slamming of LNG tank insulation panel with different impact velocities.

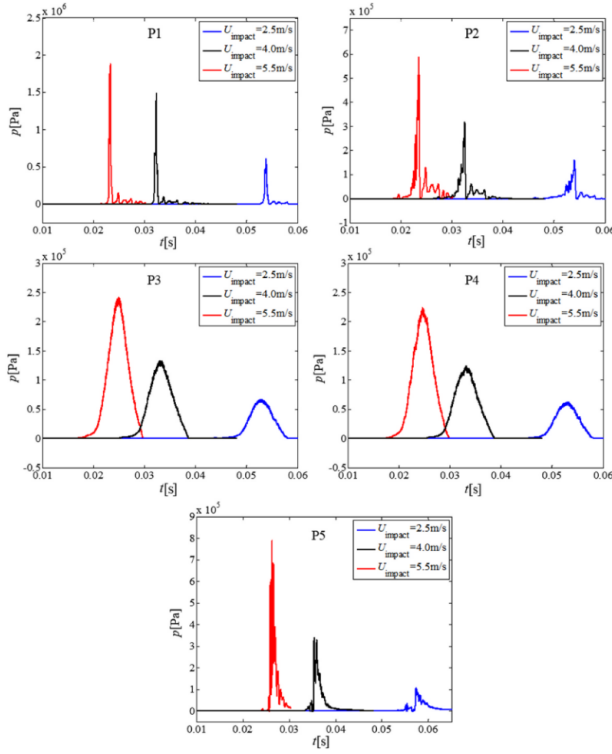


Fig. 14. Slamming of LNG tank insulation panel with different impact velocities. Time histories of the pressure of the measuring points located on the LNG tank insulation panel.

4.2.3 Influence of the deadrise angle on slamming of LNG tank insulation panel-静升角对 LNG 船绝缘板砰击的影响

In this subsection, the water slamming of the LNG tank insulation panel with different deadrise angles is simulated, and the influence of the deadrise angle on the slamming load is analyzed. The mass and initial impact velocity of the plate remain the same as those in subsection 3.2.1. Taking the left dent of the panel as center, the initial deadrise angle of the LNG tank insulation panel is adjusted to $\theta = 2^\circ$ and $\theta = 6^\circ$, respectively. Fig. 15 displays the particle distributions of the water slamming of LNG tank insulation panel with different deadrise angles. It can be observed that for the insulation panel with smaller deadrise angle, more air under the panel will be trapped, and therefore a larger air bubble is generated under the panel. When the deadrise angle ranges from 2° to 6° , the air bubble under the panel with larger deadrise angle is closer to the right side. In addition, different from the panels with deadrise angles of 2° and 4° , for the panel with deadrise angle of 6° , a small air cushion is formed between the left corner and the left dent of the panel when its left corner impacts the water as shown in the red box in Fig. 15, and then overflows the water from the left corner.

在这一小节中，模拟了不同静升角下的 LNG 船绝缘板与水的砰击，并分析了静升角对砰击载荷的影响。板的质量和初始砰击速度保持与 subsection 3.2.1 中相同。以板的左齿为中心，调整 LNG 船绝缘板的初始静升角分别为 $\theta = 2^\circ$ 和 $\theta = 6^\circ$ 。Fig. 15 给出了不同静升角的 LNG 船绝缘板与水砰击的粒子分布。可以看出越小的静升角的绝缘板能够困住更多的空气，因此板底生成了更大的气泡。当静升角从 2° 到 6° ，越大的静升角下的板底的气泡越靠近右侧。此外，与静升角 2° 和 4° 下的板不同，对于静

升角 6° , 当左角砰击水面时, 在左角和左齿间形成了一个更小的气垫, 如 Fig. 15 红框所示, 随后从左角溢出水。

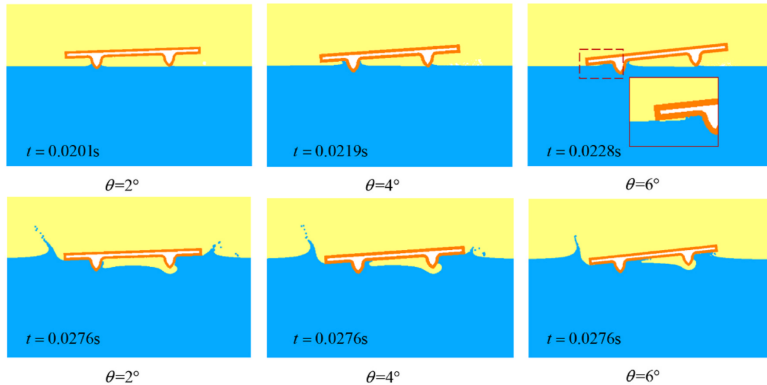


Fig. 15. Particle distributions of the water slamming of LNG tank insulation panel with different deadrise angles.

Fig. 16 gives the time histories of the pressure of the five measuring points on the panel with different deadrise angles. It can be found that generally, the slamming pressure peak of the point on the panel with a smaller deadrise angle is lower. Specifically, for points P3, P4 and P5, because the larger deadrise angle makes these measuring points on panel farther from the water surface, it is found that the time histories of pressure of these measuring points on the panel with a larger deadrise angle are more lagging with a larger peak. In particular, for points P3 and P4, the pulse width of their time histories of pressure on the panel with larger deadrise angle is significantly reduced due to the smaller air bubble formed under the plate. For points P1 and P2, the pressure peak of the panel with a larger deadrise angle appears earlier. However, for point P1, the variation trend of its pressure peak is different. It can be found that the pressure peak of the panel with the deadrise angle of 6° is smaller than that of the panel with the deadrise angle of 4° and close to that of the panel with the deadrise angle of 2° owing to the small air cushion formed below the point P1.

Fig. 16 给出了不同静升角下板上五个测量点压力的时间历程。可以发现通常情况下, 静升角越小的板的砰击压力峰值越小。具体来说, 对于点 P3,P4,P5, 因为越大的静升角使这些测量低与水面越远, 可以发现越大静升角上测量点的时间历程有越大且越滞后的压力峰值。特别地, 对于点 P3 和 P4, 由于板下形成的气泡越小, 越大的静升角其板上压力的时间历程的脉冲宽度大幅减小。对于点 P1 和 P2, 更大静升角的板的压力峰值出现得更早。然而, 对点 P1, 其压力峰值的变化趋势是不同的。可以看出静升角 6° 下板压力峰值小于静升角 4° 下板的压力峰值, 并接近静升角 2° 下板的压力峰值, 这是因为点 P1 下形成的小气垫。

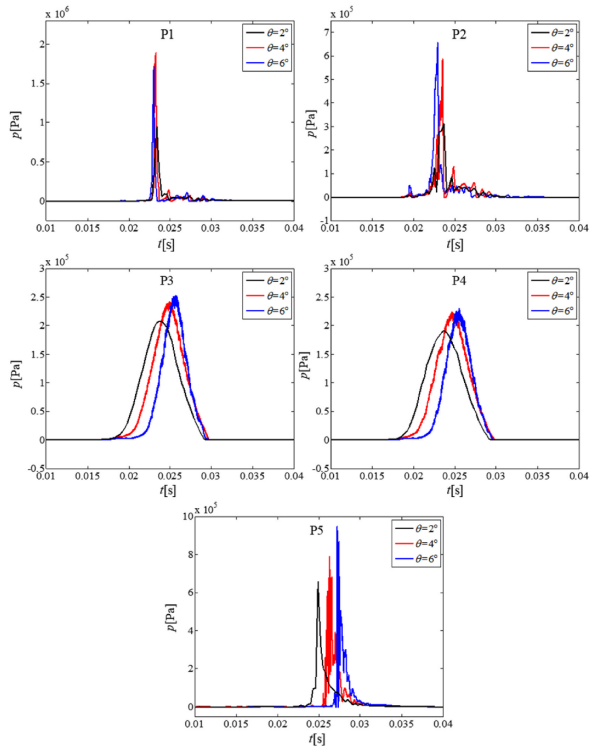


Fig. 16. Slamming of LNG tank insulation panel with different deadrise angles. Time histories of the pressure of the measuring points located on the LNG tank insulation panel.

5 conclusions

In this work, the multiphase Riemann-SPH method is adopted to study the air-cushion effect and slamming load in water entry. Through the test of slamming of a flat plate, the accuracy and convergence of the adopted method are validated, and then the influences of the air cushion and the plate length on the slamming load are discussed. Results show that for the water entry problem involving the air cushion, the buffering effect of the air is vital for the accurate prediction of the slamming load, and ignoring the air will largely overestimate the peak of the slamming load. For the water slamming of the plate, with the increase of plate length, the contact area between the plate and the water increases, which results in the larger slamming load of the plate but more obvious buffering effect of the air cushion. That is, for the longer plate, the slamming force peak of the plate will decrease in a larger proportion due to the existence of air.

本文中，采用多相黎曼-SPH 方法研究入水过程中的气垫效应和砰击载荷。通过平板砰击实验，验证了所采用方法的精确性和收敛性，随后讨论了气垫和板长对于砰击载荷的影响。结果表明包含气垫的入水问题，空气的缓冲效应对砰击载荷的精确预测至关重要，忽略空气将极大地过高估计砰击载荷的峰值。对于平板与水的砰击，随着板长的增加，板和水间的接触面积增大，会导致更大的板的砰击载荷，但更明显的气垫缓冲效应。即板长越长，对于越长的板，由于空气的存在，其砰击载荷的峰值将会减小。

Besides, focusing on the air-cushion effect in the water entry, the slamming of a LNG tank insulation panel is simulated. It is demonstrated that the air-cushion effect has a great influence on the time-space dis-tributions of the slamming loads. The peak of the slamming pressure increases with the increase of the impact velocity, while the change of the impact velocity has little influence on the formation position of air cushion when the impact velocity ranges from 2.5m/s to 5.5m/s. For the study on the panels with different deadrise angles, it is found that generally, for the panel with a smaller deadrise angle, the buffering effect of the air cushion is more significant and thus leading to lower slamming pressure peak. Furthermore, the change of the deadrise angle of the structure will influence the position of the air bubble generated under the panel and further affect the local slamming loads of the structure.

此外，本文模拟了 LNG 船绝缘板的砰击，重点研究了入水过程中的气垫效应。研究证实了气垫效应对砰击载荷的时空分布有极大的影响。砰击压力的峰值随着砰击速度的增大而增大，然而当砰击速度在 2.5m/s 到 5.5m/s 间，砰击速度的变化对气垫的生成位置影响较小。对于研究不同静升角下的面板，可以看出一般而言，对于越小的静升角下的板，气垫的缓冲效应更显著，因此导致了更低的砰击压力峰值。此外，静升角的变化将会影响到板底气泡的生成，并进一步影响结构物的砰击载荷。

6 Appendix A:The test of the slamming of Mark-III panel

In this section, the slamming of the Mark-III type insulation panel carried out by Marrone et al. (2017) is tested. The sketch of the numerical model is shown in Fig. 17. In order to save the computational cost, this panel was initially placed 0.56 m above the water surface. The impact velocity and the deadrise angle of the panel are $U_{impact} = 6m/s$ and $\theta = 4^\circ$, respectively. In the present simulation, the particle spacing Δx is set to 0.002 m. Different from the use of Mach number $Ma = U_{impact}/c_{water} = 0.1$ in Marrone et al. (2017), $Ma = U_{impact}/c_{water} = 0.015$ is adopted in the present simulation. Similar to Marrone et al. (2017), for easy to compare, the time coordinate of the numerical results is translated to make it consistent with the experimental data in Marrone et al. (2017).

在本节中，实验了 Marrone et al.(2017) 提出的 Mark-III 型绝缘板的砰击。数值模型的示意图如 Fig. 17 所示。为节省计算开销，该板初始被放置在距水面 0.56m 的高度。板的砰击速度和静升角分别为 $U_{impact} = 6m/s$ 和 $\theta = 4^\circ$ 。在当前模拟中，粒子的间距 Δx 设置为 0.002m. 与 Marrone et al.(2017) 所用的马赫数 $Ma = U_{impact}/c_{water} = 0.1$ 不同，本次采用了 $Ma = U_{impact}/c_{water} = 0.015$. 和 Marrone et al.(2017) 类似，为便于比较，平移了数值结果的时间坐标，使之与实验数据 (2017) 相一致。

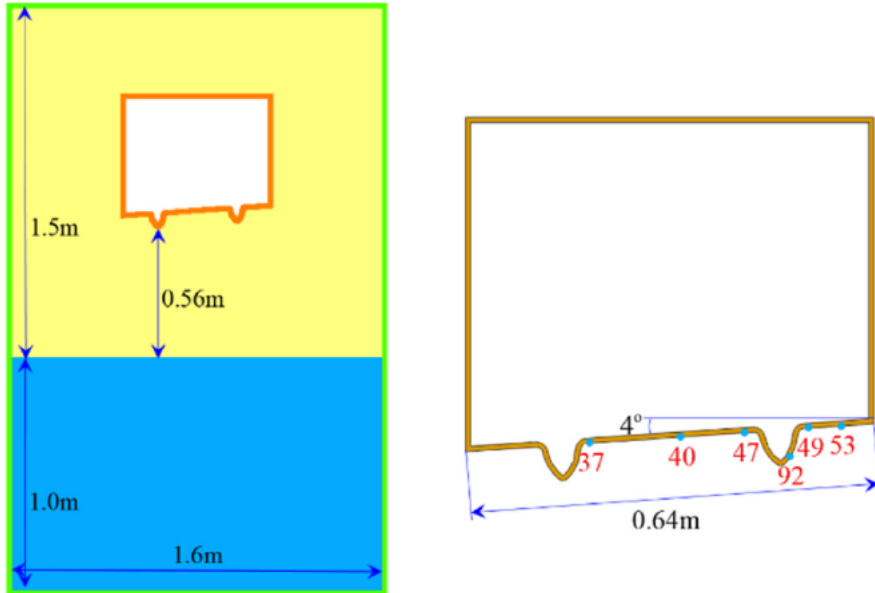


Fig. 17. Sketch of the slamming of the Mark-III type insulation panel.

Fig. 18 shows the particle distributions and corresponding pressure fields at three typical time instants. It can be observed that when the left corner of the panel impacts the water, a violent impact pressure wave is produced. With the fall of the panel, the trapped air forms a bubble under the panel. Since the air inside the bubble is compressed, a small high-pressure area is formed under the panel. As the air bubble expands and overflows from the right dent, the bubble pressure becomes lower. In general, the present results can capture the flow pattern of the air cushion under the panel and obtain a relatively smooth pressure field. However, when the water slams onto the structure, there are some pressure noise generated in the local area.

Fig. 18 给出了三个典型时刻的粒子分布和相应的压力场信息。可以看到当板的左角砰击到水面，产升了猛烈的砰击压力波。随着板的下落，被困的空气在板下形成了气泡。由于气泡内空气被压缩，一小片高压区域在板下形成。当气泡膨胀并从右齿处逸出，气泡内压力变低。总而言之，本文的结果可以捕捉板下气垫的流动模式和相对光滑的压力场。然而，当水砰击到结构物时，在局部区域会形成一定的压力噪

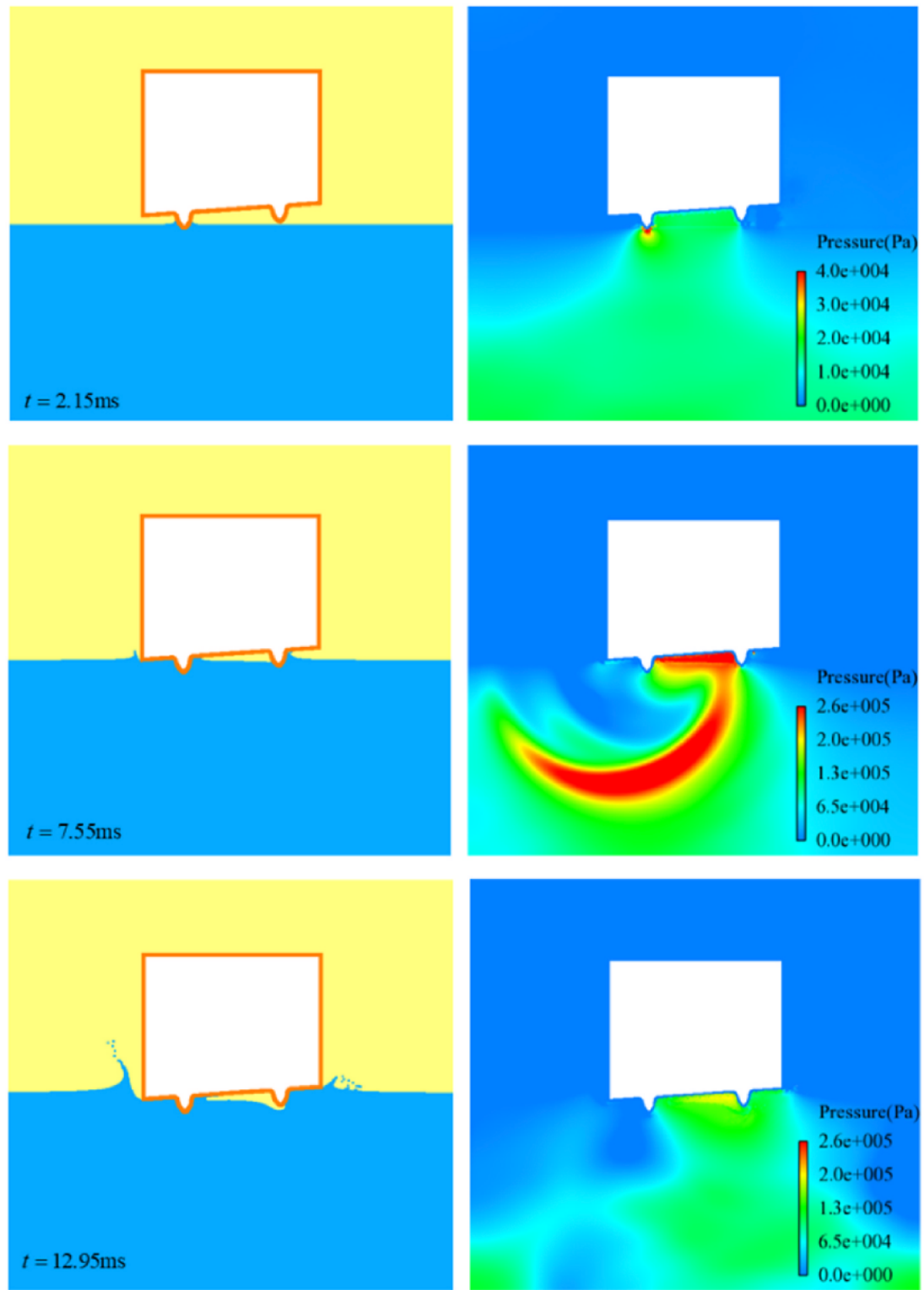


Fig. 18. Slamming of the Mark-III type insulation panel. Particle distributions (left) and pressure fields (right) at three instants.

声。

Fig. 19 gives the time histories of the pressure of the six measuring points on the panel, and it can be found that generally, compared with the Riemann-ALE SPH results of Marrone et al. (2017), the pressure peaks of measuring points predicted by the present SPH are larger and the pulse widths are smaller, which are closer to the experimental results of Marrone et al. (2017). This can be attributed to two reasons. On the one hand, a larger water speed of sound is adopted in the present simulation with respect to the one used by Marrone et al. (2017). Therefore, the compressibility of water is weaker in the present work, and when the structure impacts on the water, the present pressure time histories are relatively sharper with larger peak values. On the other hand, owing to the use of the dissipation limiter, the dissipation introduced by the Riemann solver is reduced greatly, and the numerical viscosity of fluid is lower in the present simulation, which also increases the pressure peaks to some extent. However, compared with the smooth pressure evolution obtained by Riemann-ALE SPH in Marrone et al. (2017) Marrone et al. (2017), more severe oscillations are displayed in the present results, especially for the measuring points 49, 53 and 92, which can also be attributed to the adopted larger water speed of sound and the use of the dissipation limiter in the present Riemann SPH.

Fig. 19 给出了板上六个测量点压力的时间历程，可以看出，总体上，与 Marrone et al.(2017) 的黎曼-ALE SPH 结果相比，本文 SPH 方法预测的测量点压力峰值更大且脉冲宽度更小，更接近于 Marrone et al(2017) 的实验数据。这可以归因于两个原因。一方面是本文的模拟使用了比 Marrone et al. (2017) 所使用的更大的水声速。因此，在本文中水的可压缩性更弱，当结构物碎击水时，本文的压力时间历程相对尖锐，峰值较大。另一方面，因为使用了耗散限制器，极大减少了由黎曼求解器产生的耗散，并且当前模拟中的数值粘度更低，这在一定程度上也增大了压力峰值。然而，与 Marrone et al.(2017) 中的黎曼-ALE SPH 所获得的光滑压力变化相比，本文的结果给出了更严重的震荡，特别是对于测量点 49, 53 和 92，这也归因于在当前 SPH 方法中应用了更高的水声速和使用了耗散限制

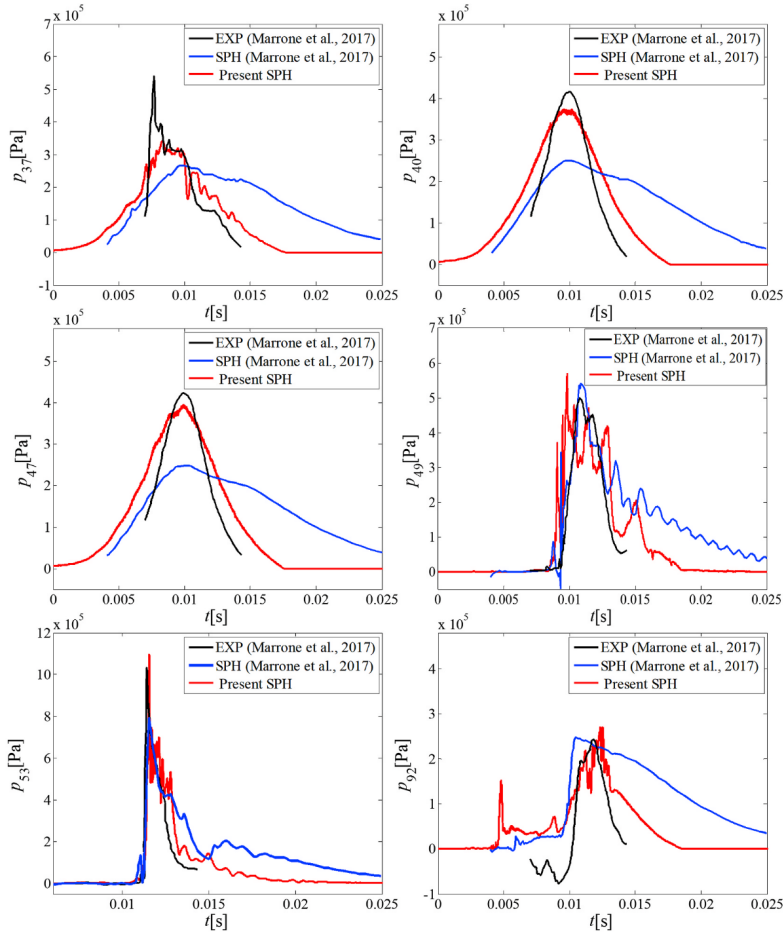


Fig. 19. Time histories of the pressure of the measuring points located on the Mark-III type insulation panel.

HFF

References

- Adami, S., Hu, X., Adams, N.A., 2012. A generalized wall boundary condition for smoothed particle hydrodynamics. *J. Comput. Phys.* 231 (21), 7057–7075.
- Antuono, M., Colagrossi, A., Marrone, S., Molteni, D., 2010. Free-surface flows solved by means of SPH schemes with numerical diffusive terms. *Comput. Phys. Commun.* 181 (3), 532–549.
- Chen, Z., Zong, Z., Liu, M.B., Zou, L., Li, H.T., Shu, C., 2015. An SPH model for multiphase flows with complex interfaces and large density differences. *J. Comput. Phys.* 283, 169–188.
- Cheng, H., Ming, F.R., Zhang, A.M., 2017. Numerical simulation of water-entry problems using an improved multiphase SPH method. In: Proc. 12th SPHERIC Workshop.
- Chuang, S.L., 1966. Experiments on flat-bottom slamming. *J. Ship Res.* 10 (1), 10–17.
- Colagrossi, A., Landrini, M., 2003. Numerical simulation of interfacial flows by smoothed particle hydrodynamics. *J. Comput. Phys.* 191 (2), 448–475.
- Gong, K., Shao, S., Liu, H., Wang, B., Tan, S.K., 2016. Two-phase SPH simulation of fluid-structure interactions. *J. Fluid Struct.* 65, 155–179.
- Gong, K., Shao, S., Liu, H., Lin, P., Gui, Q., 2019. Cylindrical smoothed particle hydrodynamics simulations of water entry. *J. Fluid Eng.* 141 (7), 071303.
- Grenier, N., Antuono, M., Colagrossi, A., Le Touzé, D., Alessandrini, B., 2009. An Hamiltonian interface SPH formulation for multi-fluid and free surface flows. *J. Comput. Phys.* 228 (22), 8380–8393.
- Hammani, I., Marrone, S., Colagrossi, A., et al., 2020. Detailed study on the extension of the 8 -SPH model to multi-phase flow. *Comput. Methods Appl. Mech. Eng.* 368, 113189.
- Kazemi, E., Koll, K., Tait, S., Shao, S., 2020. SPH modelling of turbulent open channel flow over and within natural gravel beds with rough interfacial boundaries. *Adv. Water Resour.* 103557.
- Khayyer, A., Gotoh, H., 2016. A multiphase Compressible-Incompressible particle method for water slamming. *Int. J. Offshore Polar Eng.* 26 (01), 20–25.
- Khayyer, A., Gotoh, H., Shimizu, Y., 2017. Comparative study on accuracy and conservation properties of two particle regularization schemes and proposal of an optimized particle shifting scheme in ISPH context. *J. Comput. Phys.* 332, 236–256.
- Khayyer, A., Gotoh, H., Shimizu, Y., 2019. A projection-based particle method with optimized particle shifting for multiphase flows with large density ratios and discontinuous density fields. *Comput. Fluid* 179, 356–371.

- Khayyer, A., Shimizu, Y., Gotoh, H., et al., 2021. Multi-resolution ISPH-SPH for accurate and efficient simulation of hydroelastic fluid-structure interactions in ocean engineering. *Ocean Eng.* 226, 108652.
- Lee, E.S., Moulinec, C., Xu, R., Violeau, D., Laurence, D., Stansby, P., 2008. Comparisons of weakly compressible and truly incompressible algorithms for the SPH mesh free particle method. *J. Comput. Phys.* 227 (18), 8417–8436.
- Leffe, M., Le Touzé, D., Alessandrini, B., 2009. Normal Flux Method at the Boundary for SPH. 4th International Spheric Workshop, pp. 149–156.
- Lewison, G., 1968. On the cushioning of water impact by entrapped air. *J. Ship Res.* 12 (2), 116–130.
- Lind, S.J., Xu, R., Stansby, P.K., Rogers, B.D., 2012. Incompressible smoothed particle hydrodynamics for free-surface flows: a generalised diffusion-based algorithm for stability and validations for impulsive flows and propagating waves. *J. Comput. Phys.* 231 (4), 1499–1523.
- Lind, S.J., Stansby, P.K., Rogers, B.D., M, L.P., 2015. Numerical predictions of water-air wave slam using incompressible-compressible smoothed particle hydrodynamics. *Appl. Ocean Res.* 49, 57–71.
- Liu, M.B., Zhang, Z.L., 2019. Smoothed particle hydrodynamics (SPH) for modeling fluid-structure interactions. *Sci. China Phys. Mech. Astron.* 62 (8), 5–42.
- Liu, X., Lin, P., Shao, S., 2014. An ISPH simulation of coupled structure interaction with free surface flows. *J. Fluid Struct.* 48, 46–61.
- Ma, Z.H., Causon, D.M., Qian, L., Mingham, C.G., Gu, H.B., Ferrer, P.M., 2014. A compressible multiphase flow model for violent aerated wave impact problems. *Proc. Roy. Soc. Math. Phys. Eng. Sci.* 470 (2172), 0542.
- Ma, Z.H., Causon, D.M., Qian, L., Mingham, C.G., Mai, T., Greaves, D., Raby, A., 2016. Pure and aerated water entry of a flat plate. *Phys. Fluids* 28 (1), 016104.
- Marrone, S., Colagrossi, A., Le Touzé, D., Graziani, G., 2010. Fast free-surface detection and level-set function definition in SPH solvers. *J. Comput. Phys.* 229 (10), 3652–3663.
- Marrone, S., Colagrossi, A., Park, J.S., Campana, E.F., 2017. Challenges on the numerical prediction of slamming loads on LNG tank insulation panels. *Ocean Eng.* 141, 512–530.
- Marrone, S., Colagrossi, A., Chiron, L., Leffe, M., Le Touzé, D., 2018. High-speed water impacts of flat plates in different ditching configuration through a Riemann-ALE SPH model. *J. Hydraul. Dyn.* 30, 38–48.
- Meng, Z.F., Wang, P.P., Man Zhang, A., Ming, F.R., Sun, P.N., 2020. A multiphase SPH model based on Roe's approximate Riemann solver for hydraulic flows with complex interface. *Comput. Methods Appl. Mech. Eng.* 365, 112999.
- Ming, F.R., Sun, P.N., Zhang, A.M., 2017. Numerical investigation of rising bubbles bursting at a free surface through a multiphase SPH model. *Meccanica* 52, 2665–2684.
- Mokos, A., Rogers, B.D., Stansby, P.K., 2017. A multi-phase particle shifting algorithm for SPH simulations of violent hydrodynamics with a large number of particles. *J. Hydraul. Res.* 55, 143–162.
- Monaghan, J.J., Kajtar, J.B., 2009. SPH particle boundary forces for arbitrary boundaries. *Comput. Phys. Commun.* 180 (10), 1811–1820.
- Nasar, A.M.A., Rogers, B.D., Revell, A., Stansby, P.K., Lind, S.J., 2019. Eulerian weakly compressible smoothed particle hydrodynamics (SPH) with the immersed boundary method for thin slender bodies. *J. Fluid Struct.* 84, 263–282.
- Ng, C.O., Kot, S.C., 1992. Computations of water impact on a two-dimensional flat-bottomed body with a volume-of-fluid method. *Ocean Eng.* 19 (4), 377–393.
- Okada, S., Sumi, Y., 2000. On the water impact and elastic response of a flat plate at small impact angles. *J. Mar. Sci. Technol.* 5 (1), 31–39.
- Shao, J.R., Li, H.Q., Liu, G.R., Liu, M.B., 2012. An improved SPH method for modeling liquid sloshing dynamics. *Comput. Struct.* 100, 18–26.
- Skillen, A., Lind, S., Stansby, P., Rogers, B.D., 2013. Incompressible smoothed particle hydrodynamics (SPH) with reduced temporal noise and generalised Fickian smoothing applied to body-water slam and efficient wave-body interaction. *Comput. Methods Appl. Mech. Eng.* 265, 163–173.
- Sun, P., Colagrossi, A., Marrone, S., Zhang, A., 2017. The 8plus-SPH model: simple procedures for a further improvement of the SPH scheme. *Comput. Methods Appl. Mech. Eng.* 315, 25–49.
- Sun, P.N., Zhang, A.M., Marrone, S., Ming, F.R., 2018. An accurate and efficient SPH modeling of the water entry of circular cylinders. *Appl. Ocean Res.* 72, 60–75.
- Sun, P.N., Le Touzé, D., Oger, G., Zhang, A.M., 2021a. An accurate SPH Volume Adaptive Scheme for modeling strongly-compressible multiphase flows. Part 1: numerical scheme and validations with basic 1D and 2D benchmarks. *J. Comput. Phys.* 426, 109937.
- Sun, P.N., Le Touzé, D., Oger, G., Zhang, A.M., 2021b. An accurate SPH Volume Adaptive Scheme for modeling strongly-compressible multiphase flows. Part 2: extension of the scheme to cylindrical coordinates and simulations of 3D axisymmetric problems with experimental validations. *J. Comput. Phys.* 426, 109936.
- Toro, E.F., 2013. *Riemann Solvers and Numerical Methods for Fluid Dynamics*. Springer, Berlin.
- Über, W.H., 1932. *stoss-und gleitvorgänge an der oberfläche von flüssigkeiten*. Zeitschr. F Angew. Math. Mech. 12 (4), 193–235.
- Wang, L., Xu, F., Yang, Y., 2019a. SPH scheme for simulating the water entry of an elastomer. *Ocean Eng.* 178, 233–245.
- Wang, P.P., Zhang, A.M., Ming, F.R., Sun, P.N., Cheng, H., 2019b. A novel non-reflecting boundary condition for fluid dynamics solved by smoothed particle hydrodynamics. *J. Fluid Mech.* 860, 81–114.
- Wang, P.P., Meng, Z.F., Zhang, A.M., Ming, F.R., Sun, P.N., 2019c. Improved particle shifting technology and optimized free-surface detection method for free-surface flows in smoothed particle hydrodynamics. *Comput. Methods Appl. Mech. Eng.* 357, 112580.
- Xu, R., Stansby, P., Laurence, D., 2009. Accuracy and stability in incompressible SPH (ISPH) based on the projection method and a new approach. *J. Comput. Phys.* 228 (18), 6703–6725.
- Yang, Q.Y., Qiu, W., 2012. Numerical simulation of water impact for 2D and 3D bodies. *Ocean Eng.* 43 (4), 82–89.
- Yang, Q., Xu, F., Yang, Y., Wang, J., 2020. Two-phase SPH model based on an improved Riemann solver for water entry problems. *Ocean Eng.* 199 (2), 107039.
- Zhang, Z.L., Liu, M.B., 2018. A decoupled finite particle method for modeling incompressible flows with free surfaces. *Appl. Math. Model.* 60, 606–633.
- Zhang, C., Hu, X., Adams, N.A., 2017. A weakly compressible SPH method based on a low-dissipation Riemann solver. *J. Comput. Phys.* 335, 605–620.
- Zhang, Z., Long, T., Chang, J., Liu, M., 2019. A smoothed particle element method (SPEM) for modeling fluid-structure interaction problems with large fluid deformations. *Comput. Methods Appl. Mech. Eng.* 356, 261–293.

其中 $W_{ab} = W(|\mathbf{r}_a - \mathbf{r}_b|, h)$

$$\begin{cases} \frac{D\rho_a}{Dt} = -\rho_a \sum_b (\mathbf{u}_b - \mathbf{u}_a) \nabla_a W_{ab} V_b, \\ \frac{D\mathbf{u}_a}{Dt} = \mathbf{g} - \sum_b \left(\frac{p_a + p_b}{\rho_a} \right) \nabla_a W_{ab} V_b \end{cases} \quad (18)$$

$$\begin{cases} S1 : (\rho_L, u_L, p_L) = (\rho_b, \mathbf{u}_b \cdot \hat{\mathbf{r}}_{ab}, p_b), \\ S2 : (\rho_R, u_R, p_R) = (\rho_a, \mathbf{u}_a \cdot \hat{\mathbf{r}}_{ab}, p_a) \end{cases} \quad (19)$$

$$\begin{cases} \frac{D\rho_a}{Dt} = -2\rho_a \sum_b (\mathbf{u}^* - \mathbf{u}_a) \nabla_a W_{ab} V_b, \\ \frac{D\mathbf{u}_a}{Dt} = \mathbf{g} - 2 \sum_b \left(\frac{p^*}{\rho_a} \right) \nabla_a W_{ab} V_b \end{cases} \quad (20)$$

其中 $\mathbf{u}_L^* = \mathbf{u}_R^* = \mathbf{u}^*, p_L^* = p_R^* = p^*, \mathbf{u}_a + \mathbf{u}_b \approx 2\mathbf{u}^*, p_a + p_b \approx 2P^*, \mathbf{u}^* = u^*\hat{\mathbf{r}}_{ab} + [\frac{\mathbf{u}_a + \mathbf{u}_b}{2} - \frac{(u_L + u_R)\hat{\mathbf{r}}_{ab}}{2}], \hat{\mathbf{r}}_{ab} = \frac{\mathbf{r}_a - \mathbf{r}_b}{|\mathbf{r}_a - \mathbf{r}_b|}$

$$\begin{cases} u^* = \frac{1}{Z_L + Z_R} [Z_L u_L + Z_R u_R + (p_L - p_R)], \\ p^* = \frac{1}{Z_L + Z_R} [Z_R p_L + Z_L p_R + Z_L Z_R (u_L - u_R)] \end{cases} \quad (21)$$

其中 $Z_L = \rho_b p_b, Z_R = \rho_a p_a, (\rho_L, u_L, p_L, c_L) = (\rho_b, \mathbf{u}_b \cdot \hat{\mathbf{x}}_{ab}, p_b, c_b), (\rho_R, u_R, p_R, c_R) = (\rho_a, \mathbf{u}_a \cdot \hat{\mathbf{x}}_{ab}, p_a, c_a)$

$$p^* = \frac{1}{Z_L + Z_R} [Z_R p_L + Z_L p_R + \phi Z_L Z_R (u_L - u_R)], \quad (22)$$

其中 $\phi = \min \lambda \max[\tilde{\rho}(u_L - u_R), 0], c_{RL}/D, \tilde{\rho} = \frac{2\rho_L \rho_R}{\rho_L + \rho_R}, c_{RL} = \frac{c_R \rho_R \sqrt{\rho_R} + c_L \rho_L \sqrt{\rho_L}}{\sqrt{\rho_R} + \sqrt{\rho_L}}, \lambda = \frac{\alpha h(c_a + c_b)}{2D(u_L - u_R)|\mathbf{x}_a - \mathbf{x}_b|}, D = \frac{2Z_L Z_R}{Z_L + Z_R}, \alpha = 0.03$

$$p = \frac{c_0^2 \rho_0}{\gamma} ((\rho/\rho_0)^\gamma - 1) \quad (23)$$

$$c_0 \geq 10 \max(|\mathbf{u}_{\max}|, \sqrt{\frac{\Delta p_{\max}}{\rho_0}}) \quad (24)$$

$$\Delta t = \frac{0.25h}{c_{\max} + |\mathbf{u}_{\max}|} \quad (25)$$

$$p_d = \frac{\sum_f p_f W_{df} + \sum_f \rho_f (\mathbf{r}_f - \mathbf{r}_d)(\mathbf{a}_d - \mathbf{g}) W_{df}}{\sum_f W_{df}}, \quad (26)$$

$$\rho_d = \rho_0 \left(\frac{p_b \gamma}{c_0^2 \rho_0} + 1 \right)^{\frac{1}{\gamma}} \quad (27)$$

$$\begin{cases} \mathbf{u}_w = \mathbf{U}_0 + \mathbf{v}_0 \times \mathbf{r}_{w0}, \\ \mathbf{a}_w = \frac{D\mathbf{U}_0}{Dt} + \frac{D\mathbf{v}_0}{Dt} \times \mathbf{r}_{w0} + \mathbf{v}_0 \times \mathbf{u}_{w0} \end{cases} \quad (28)$$

$$\begin{cases} \frac{D\mathbf{U}_0}{Dt} = \frac{F_{fw}}{M} + \mathbf{g}, \\ \frac{D\mathbf{v}_0}{Dt} = \frac{\mathbf{T}_{fw}}{I} \end{cases} \quad (29)$$

$$\begin{cases} \mathbf{F}_{fw} = \sum_f \sum_w (\frac{\mathbf{r}_f + \mathbf{r}_w}{2} - \mathbf{r}_c) \times p_{fw} (V_f^2 + V_w^2) \Delta_f W_{fw}, \\ p_{fw} = \frac{\rho_w p_f + \rho_f p_2}{\rho_f + \rho_w} \end{cases} \quad (30)$$

$$\delta \mathbf{r}'_a = -A_s h |\mathbf{u}|_{\max} \Delta t \nabla C_a; \nabla C_a = \sum_b \nabla_a W_{ab} V_b, \quad (31)$$

$$\delta \mathbf{r}_a = \begin{cases} 0, & \text{if } a \in A_1, \\ (I_{\tilde{n}_a \otimes \tilde{n}_a}) \delta \mathbf{r}_a & \text{if } a \in A_2, \\ \delta \mathbf{r}'_a & \text{if } a \in A_3 \end{cases} \quad (32)$$

$$\tilde{n}_a = -\frac{B_a \cdot \Delta C_a}{|B_a \cdot \Delta C_a|}; B_a = (\sum_b \mathbf{r}_{ab} \otimes \Delta_a W_{ab} V_b)^{-1}, \quad (33)$$

$$\delta \mathbf{r}_a = \delta \mathbf{r}'_a \quad (34)$$